UNIVERSIDAD DE CONCEPCIÓN
FACULTAD DE CIENCIAS FÍSICAS Y MATEMÁTICAS

Colisiones fuera de control en cúmulos nucleares de estrellas (Runaway collisions in Nuclear Star Clusters)

Marcelo C. Vergara

Tesis presentada a la Facultad de ciencias físicas y matemáticas de la Universidad de Concepción para optar al grado académico de Magíster en Astronomía

Marzo 2022

Concepción, Chile

Profesor Guía: Dominik Schleicher (UdeC)

AGRADECIMIENTOS

Quiero agradecer a mi gato Waton Rorschach por su compañía y amor incondicional.

También quiero agradecer a mi familia. Mi madre Cynthia Vergara y mi hermano Pedro Cortés por su apoyo incondicional durante todos mis años de estudio.

También agradezco a mis profesores Dominik Schleicher, Andres Escala y Michael Fellhauer por sus comentarios para este trabajo.

Finalmente quiero agradecer al soporte financiero de ANID, desde el proyecto Millenium Nucleus NCN19_058 (TITANs). Estos recursos hicieron posible el trabajo presentado, al apoyar su desarrollo.

Resumen

Los centros de las galaxias albergan cúmulos nucleares de estrellas o agujeros negros supermasivos, o incluso ambos. Los cúmulos nucleares de estrellas son los sistemas estelares más densos y los agujeros negros supermasivos son los objetos más densos del Universo. Hay varias detecciones de agujeros negros supermasivos de alto corrimiento al rojo, sin embargo, su origen y evolución aún se desconocen. Aquí presentamos un nuevo mecanismo para formar agujeros negros supermasivos a través de colisiones en cúmulos nucleares de estrellas. Realizamos un análisis detallado de las simulaciones de N-cuerpos usando el código NBODY6++GPU para modelar la evolución en el cúmulo para 10 Myr. Los cúmulos nucleares de estrellas muestran una dinámica estelar de alta velocidad en su centro debido al profundo potencial gravitacional. Después de estos encuentros de alta velocidad, algunas estrellas pueden ser expulsadas del sistema estelar al eliminar algo de energía cinética; estas eyecciones producen una redistribución de la energía que provoca el colapso del núcleo y desencadena colisiones estelares. Eventualmente, una de estas estrellas experimentará casi todas las colisiones, convirtiéndose en el objeto más masivo del sistema. Nuestros resultados muestran que los objetos más masivos alcanzan masas del orden de $\sim 10^3$ $M_\odot$. También encontramos una eficiencia de formación de agujeros negros de alrededor de $30 - 50\%$, definida como la relación entre la masa del agujero negro y la masa estelar inicial.

Keywords –black hole: formation — methods: numerical — theory

Abstract

The centers of galaxies host nuclear star clusters or supermassive black holes, or even both. Nuclear star clusters are the densest star systems and supermassive black holes are the densest objects in the Universe. There are several detections of high redshift supermassive black holes, however, their origin and evolution are still unknown. Here we present a new mechanism for forming supermassive black holes through collisions in nuclear star clusters. We perform a detailed analysis of the N-body simulations using the code NBODY6++GPU to model the evolution in the cluster for 10 Myr. Nuclear star clusters show high-speed stellar dynamics at their center due to the deep gravitational potential. After these high-speed encounters, some stars may be ejected from the star system by removing some kinetic energy; these ejections produce a redistribution of energy that causes the core to collapse and triggers stellar collisions. Eventually, one of these stars will experience almost all of the collisions, becoming the most massive object in the system. Our results show that the most massive objects reach masses of the order of $\sim 10^3$ $M_\odot$. We also find a black hole formation efficiency of around $30 - 50\%$, defined as the ratio of the black hole mass to the initial stellar mass.

Keywords – black hole: formation — methods: numerical — theory

Contents

List of Tables

List of Figures

Chapter 1

Introduction

Supermassive black holes (SMBHs) are very compact astrophysical objects that live in the center of almost all galaxies. They can reach masses of $\sim 10^6$ $M_\odot$ to 10^9 $M_\odot$ (Volonteri, 2010), or even a few 10^{10} $M_\odot$ (Natarajan and Treister, 2009; King, 2016; Pacucci et al., 2017). These monsters are found in the local Universe and also at high redshift when the Universe was just a few hundred million years old.

The presence of these astrophysical objects in the local Universe is quite common since they have almost 12 Gyr to grow. Studies of stellar orbits confirm the presence of one of these astrophysical objects located at the center of our own galaxy the Milky Way, called Sagittarius A* (Ghez et al., 2008; Genzel et al., 2010; Gillessen et al., 2017) (see Fig. 1.0.1). The SMBH has a symbiotic evolution with its host galaxy since there are observed correlations between the mass of the galaxy and the mass of the SMBH (Magorrian et al., 1998; Marconi and Hunt, 2003; Häring and Rix, 2004) and also between the stellar velocity dispersion and the mass of the SMBH (Ferrarese and Merritt, 2000; Tremaine et al., 2002; McConnell and Ma, 2013; Gültekin et al., 2009; Lützgendorf et al., 2013).

On the other hand, the origin of SMBHs at high redshift ($z \geq 5$) is still unclear, since they had just one billion years to grow and reach billions of solar masses. Some observations of these monsters are the discovery of three quasars at $z > 6$ by Fan et al. (2003), also the ULAS J112'+0641 at redshift $z = 7.085$ with a mass of 2×10^9 $M_\odot$ by Mortlock et al. (2011). The observation of three quasars at z > 6.5 with masses of around $(1 - 2) \times 10^9$ $M_\odot$ (Venemans et al., 2013). Bañados

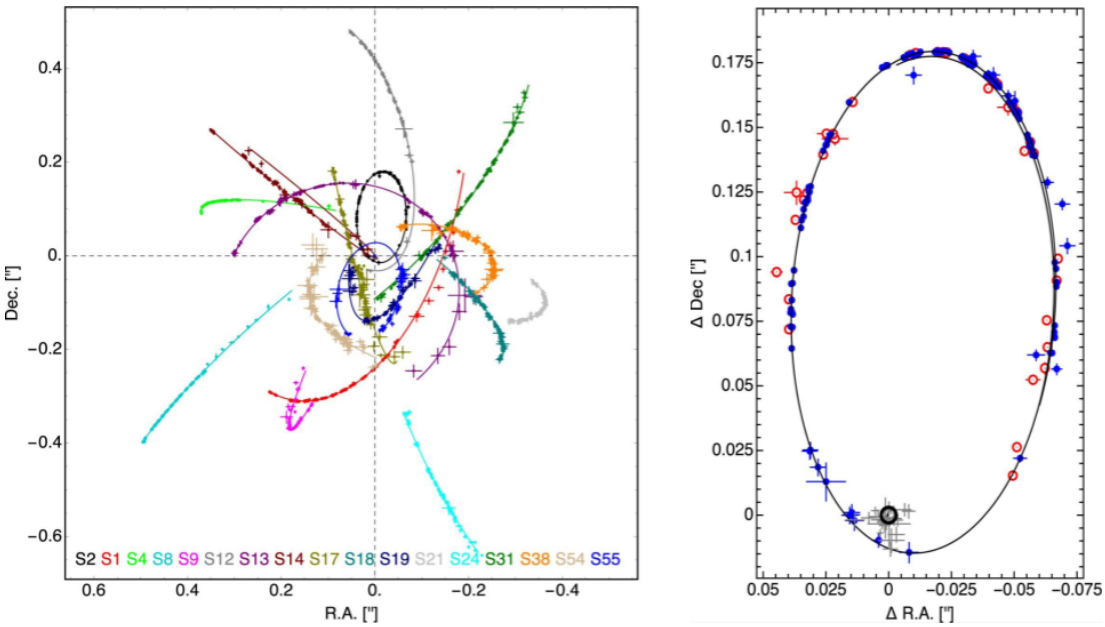

Figure 1.0.1: Left panel: 17 S-stars orbits around Sagittarius A*. Right panel: orbit of S2 star around Sagittarius A*.

Source: Gillessen et al. (2017).

et al. (2016) studied the properties of more than 100 quasars at high redshift $5.6 \lesssim z \lesssim 6.7$. There is also the quasar, SDSS J010013.02+280225.8, discovered by Wu et al. (2015) at redshift $z = 6.3$ with a mass of 1.2×10^{10} $M_\odot$ and the most distant AGN at $z = 7.5$ with a mass of 8×10^8 $M_\odot$ (Bañados et al., 2018). Also in the 10^6 $M_\odot$ range, several SMBHs at high redshift have been found (Onoue et al., 2019; Shen et al., 2019; Wang et al., 2019; Li et al., 2020; Pensabene et al., 2021).

As the recent observation of the supermassive object in M87 by the Event Horizon Telescope (EHT) (Event Horizon Telescope Collaboration et al., 2019) indeed confirmed that it is a black hole, we will generally assume in this thesis that the central massive objects are black holes Fig. 1.0.2.

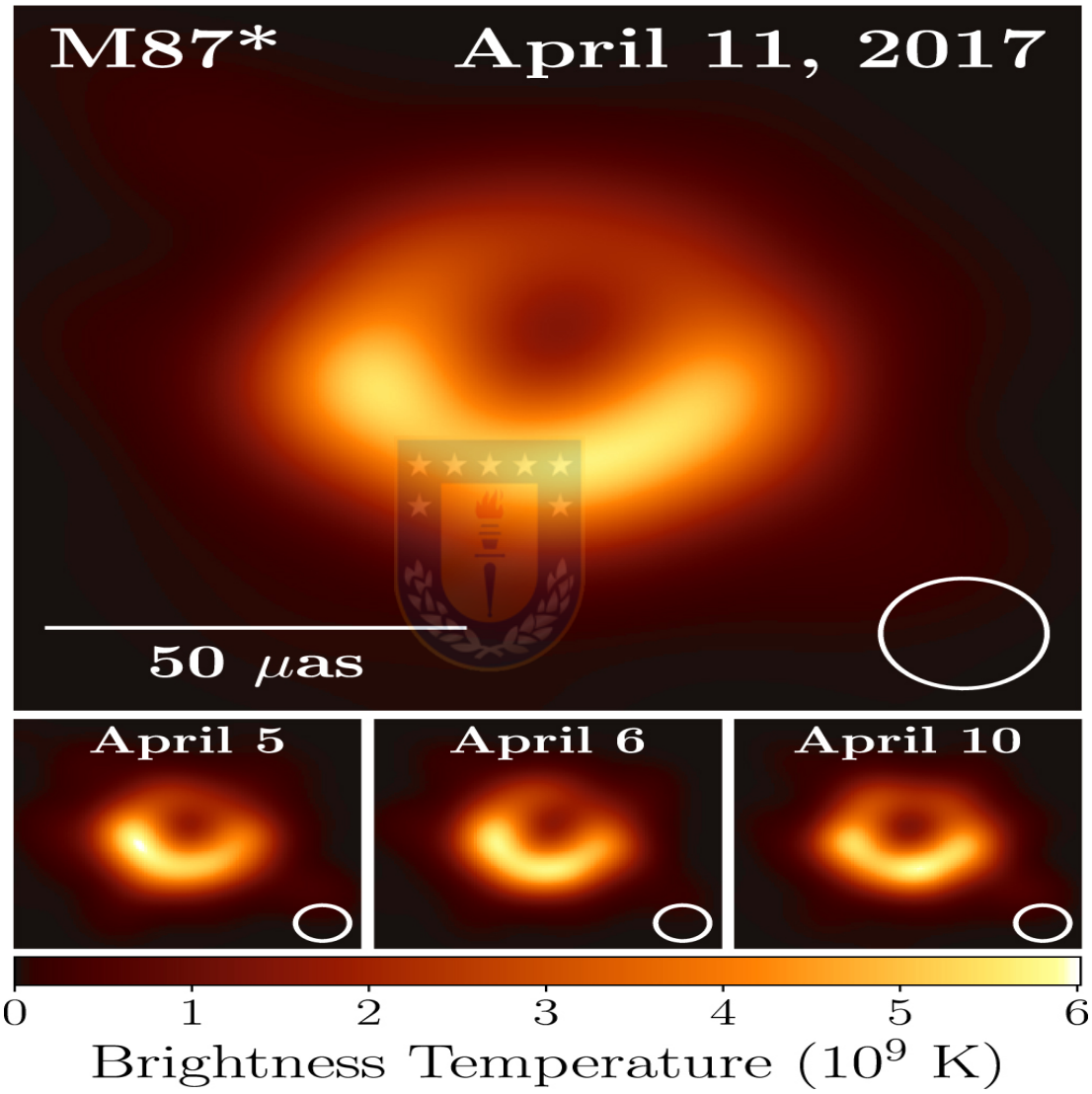

Figure 1.0.2: First image of the SMBH in M87.

Source: Event Horizon Telescope Collaboration et al. (2019).

1.1 Supermassive black holes

The formation of SMBHs and their evolution is not clear. However, there are some pathways to explain their origin (Rees, 1984; Volonteri, 2010; Woods et al., 2019).

One of the pathways is based on the remnants of population III stars (Pop. III). These stars are born in clouds with zero metallicity. Several simulations about the collapse of primordial clouds show that the first stars can be composed of many very massive stars (VMS) (Madau and Rees, 2001; Bromm et al., 2002; Yoshida et al., 2006; Gao et al., 2007; Clark et al., 2011; Greif et al., 2012; Hirano et al., 2014; Stacy et al., 2016). Even when the cloud collapses, stars can accumulate material over the hydrostatic core of the protostar, forming VMSs (Omukai and Nishi, 1998; Volonteri et al., 2003; Tan and McKee, 2004; Sakurai et al., 2020; Parsons et al., 2021). An alternative pathway is the Direct Collapse (DC), which consists of the collapse of a massive gas cloud in a cold atomic cooling halo at high redshift (Bromm and Loeb, 2003; Koushiappas et al., 2004; Begelman et al., 2006; Wise et al., 2008; Volonteri et al., 2008a; Schleicher et al., 2010a; Latif et al., 2013; Latif and Schleicher, 2015; Regan et al., 2017; Grete et al., 2019; Suazo et al., 2019; Chon and Omukai, 2020; Latif et al., 2021). This process requires inflows rates around 0.1 $M_{\odot}/yr$ (Begelman, 2010; Schleicher et al., 2013; Sakurai et al., 2015). These inflow rates require a strong Lyman Werner (LW) flux to prevent the formation of molecular hydrogen (Omukai, 2000; Schleicher et al., 2010b; Latif et al., 2014) since the presence of contaminants such as metals, dust, or molecular hydrogen can cause fragmentation in the cloud (Schneider et al., 2006; Omukai et al., 2008; Clark et al., 2008; Schneider and Omukai, 2010; Peters et al., 2014; Bovino et al., 2014, 2016; Latif et al., 2016; Grassi et al., 2017). Another proposed pathway is based on the runaway collision and mergers of stars in a cluster (Portegies Zwart and McMillan, 2002; Devecchi and Volonteri, 2009; Katz et al., 2015; Sakurai et al., 2017, 2019; Boekholt et al., 2018; Reinoso et al., 2018, 2020; Alister Seguel et al., 2020; Tagawa et al., 2020; Das et al., 2021; Vergara et al., 2021; Escala, 2021); in this scenario, the most massive star sinks to the center of the cluster due to the conservation of momentum and equipartition of energy during direct collisions. The new object has a larger collisional cross-section than other stars in the cluster, increasing the rate of collisions and mergers.

Fig. 1.1.1 shows a diagram summarizing the principal pathways of black hole formation.

A more exotic pathway is proposed by Davies et al. (2011); Lupi et al. (2014); O'Leary et al. (2016); Antonini et al. (2019); Kroupa et al. (2020), in which the formation of supermassive black holes occurs through stellar black hole collisions and mergers.

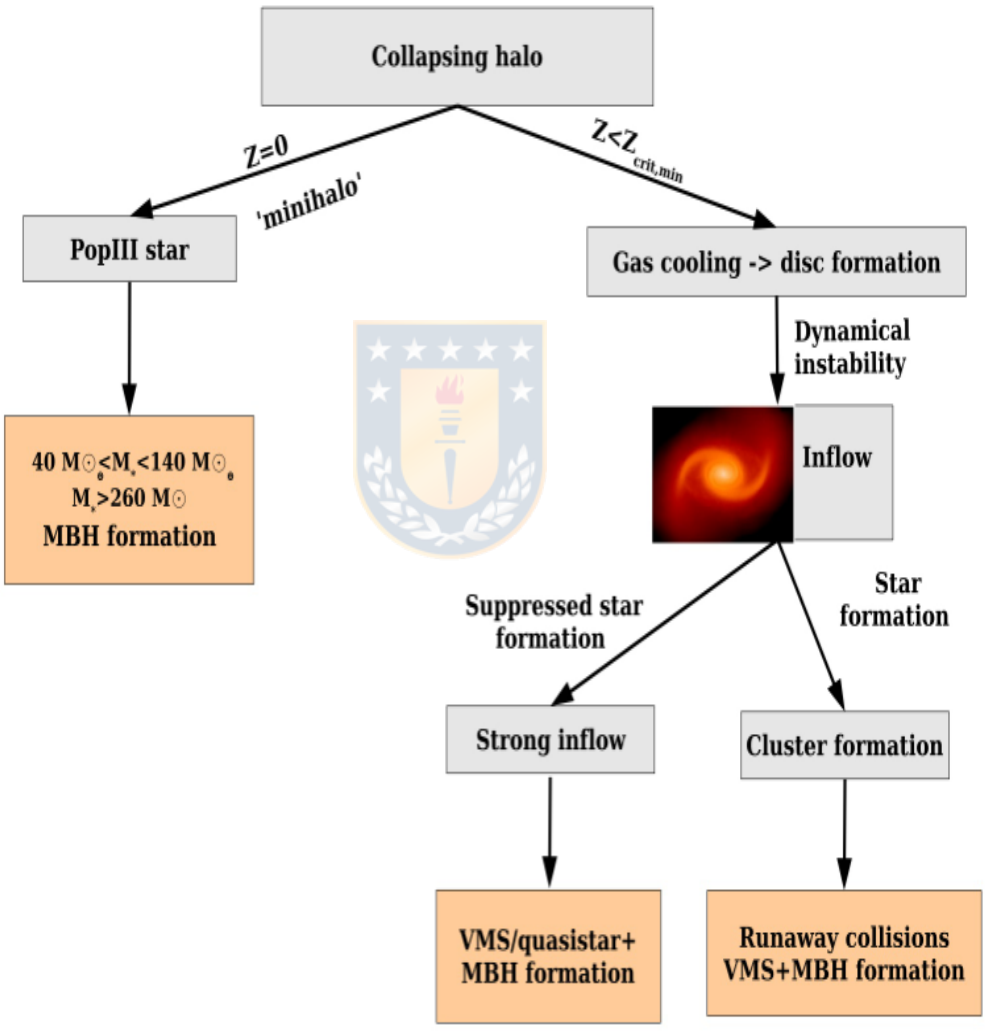

Figure 1.1.1: Summary of the pathways to black hole formation.

Source: Volonteri (2010).

1.2 Nuclear Star Cluster and Central Massive Objects

The Nuclear Star Clusters (NSC) are the densest stellar systems in nature (Böker et al., 2002; Côté et al., 2006) (see Fig. 1.2.1). The centers of galaxies can host a NSC (Böker et al., 2002; Côté et al., 2006) or a massive black hole (MBH) (Kormendy and Ho, 2013). If the galaxy has a mass of 10^{10} $M_{\odot}$ or 10^{12} $M_{\odot}$, respectively, it can even host both (Georgiev et al., 2016). There are findings of a correlation between the mass of the galaxy and the mass of the NSC or/and MBH (Ferrarese et al., 2006; Wehner and Harris, 2006; Li et al., 2007; Graham and Spitler, 2009; Genzel et al., 2010; Leigh et al., 2012; Antonini et al., 2015). The coexistence of the NSC and the MBH is sometimes called Central Massive Object (CMO) (Ferrarese et al., 2006).

Our own galaxy, the Milky Way, hosts a CMO (Genzel et al., 2010; Schödel et al., 2014). There is also a CMO at the center of M31 (Bender et al., 2005), NGC 4395 (Filippenko and Ho, 2003), NGC 1042 (Shields et al., 2008), NGC 3621 (Barth et al., 2009) and NGC 404 (Seth et al., 2010; Nguyen et al., 2017). These investigations point towards NSC and MBH having a common origin, with different evolutionary histories.

1.3 Relaxation and collision timescales

Close encounters of stars within the cluster generally occur at high speed in the center of the cluster due to the deep gravitational potential. These gravitational interactions can lead to the ejection of stars that leave the system with some kinetic energy producing a redistribution of energy, allowing the cluster to undergo a core collapse (Lynden-Bell and Wood, 1968; Cohn, 1979; Spitzer, 1987). Stellar collisions are expected to occur when the cluster core collapses, triggering an object to experience almost all of the collisions, increasing exponentially in mass during the core collapse (Portegies Zwart et al., 1999; Portegies Zwart and McMillan, 2002). Core collapse has an associated time known as the relaxation timescale. If the system is virialized, the crossing time is $t_{cross} = \sqrt{R^3/GM}$, where G is the gravitational constant, R and M are the radius and mass of the cluster , respectively. The crossing time quantifies the time of a star with a typical velocity

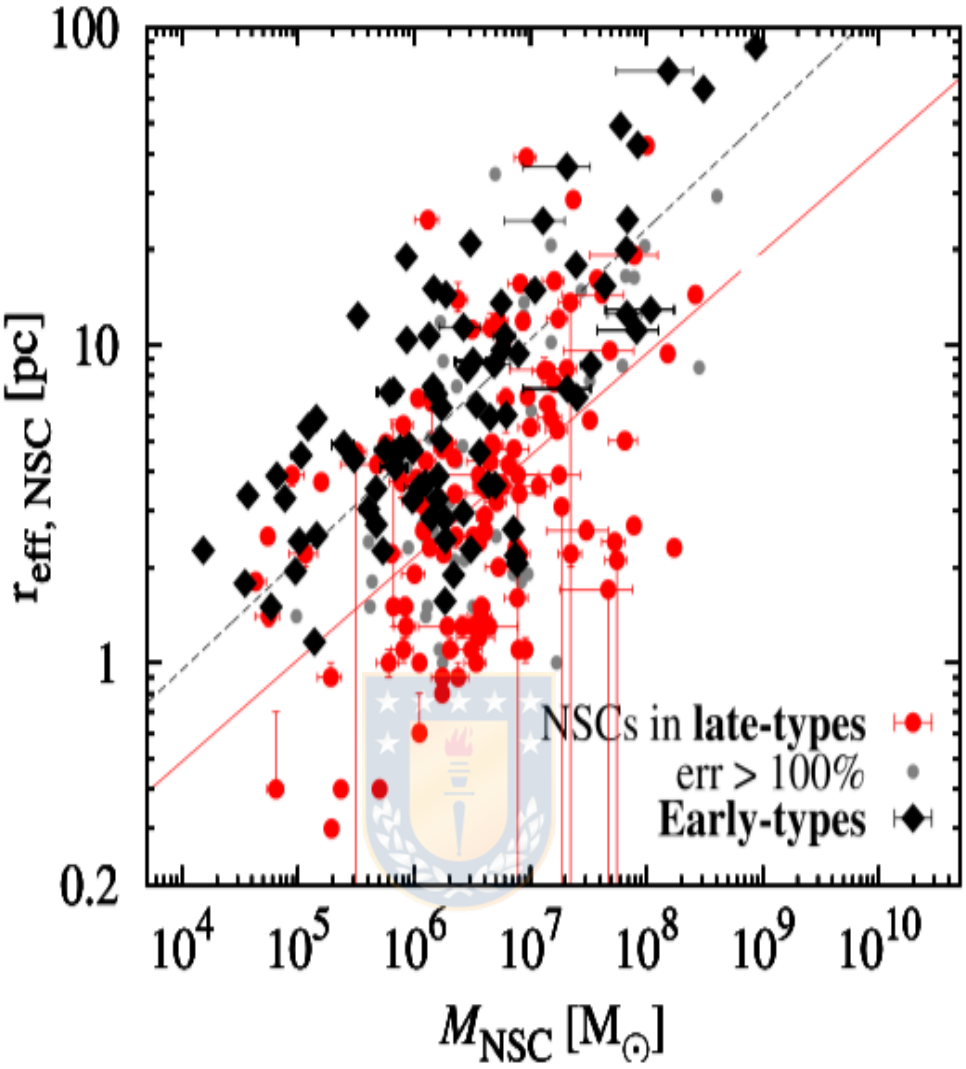

Figure 1.2.1: Size-mass relation of NSCs in early and late type host galaxies.

Source: Georgiev et al. (2016).

to cross the cluster. The typical velocity is just defined as the root square mean of the stellar velocities. The relaxation timescale is related to the perturbation of the global properties of the cluster such as the stellar orbits; in addition, it quantifies the energy exchange between two bodies. Binney and Tremaine (2008) defined the relaxation timescale as

$$t_{relax} = \frac{0.1N}{\ln N}\sqrt{\frac{R^3}{GM}} = \frac{0.1N}{\ln N}t_{cross}, \tag{1.3.1}$$

where N is the total number of particles. If the cluster has stars of equal mass,

the number of stars is defined as $N = M/\eta$, where η represents the mass of a single star.

In a cluster with stars of equal mass η the occurrence of runaway collisions can be quantified according to Binney and Tremaine (2008) as $t_{coll} = \lambda/\sigma$, where σ is the dispersion velocity and λ is the particle mean free path. In a virialized system the dispersion velocity is defined as $\sigma = \sqrt{GM/R}$. Also Landau and Lifshitz (1980) and Shu (1991) define a probabilistic mean free path as $\lambda = 1/n\Sigma_0$, where Σ_0 is the effective cross section and n is the number density of stars, therefore the collision rate is defined as

$$t_{coll} = \frac{1}{n\Sigma_0}\sqrt{\frac{R}{GM}}, \tag{1.3.2}$$

the number density is $n = 3M/4\pi R^3\eta$ and according Leigh et al. (2012) the effective cross section is $\Sigma_0 \approx 100\pi\xi^2$, for $\sigma \sim 100$ km/s.

1.4 Quantification of collisions in NSC

Star clusters are prone to collisions. Numerical simulations show that runaway collisions of massive stars allow the formation of Intermediate-Mass Black Holes (IMBHs) with masses $\sim 10^3 M_\odot$ in a typical globular cluster (Portegies Zwart and McMillan, 2002; Devecchi and Volonteri, 2009; Sakurai et al., 2017; Reinoso et al., 2018). Unfortunately, it is not yet known what happens in an extreme environment like a NSC due to the lack of N-body simulations as they are very expensive (Escala, 2021).

Under the condition that the collision timescale is comparable to or shorter than the Hubble time (t_H), Escala (2021) derived the following equation the equation 1.3.2;

$$\rho_{crit} \equiv \left(\frac{4\eta}{300\xi^2 t_H G^{1/2}}\right) \leq MR^{-7/3}, \tag{1.4.1}$$

ρ_{crit} is the critical mass density, a density between the volumetric density ($\propto R^{-3}$) and the surface density ($\propto R^{-2}$), the value of t_H follows the order of magnitude of the age of the Universe $\sim 10^{10}$ yr (Spergel et al., 2003) leading to a minimal

critical mass density $\rho_{crit} \sim 10^7 \mathrm{M}_\odot \mathrm{pc}^{-7/3}$. η and ξ are the mass and radius of the stars.

It is well known that in a virialized system $R = GM/\sigma^2$, therefore equation 1.4.1 can be rewritten according Escala (2021) as

$$\sqrt{\frac{4\eta}{300\sigma_\odot \mathrm{t_H}}} \leq \frac{\eta}{M}\left(\frac{\sigma}{\sigma_\odot}\right)^{7/2}. \tag{1.4.2}$$

If $\sigma_\odot = \sqrt{G\eta/\xi} \sim 400$ km/s and considering the empirical scaling relation from (Leigh et al., 2012), $M_{NSC}/10^{6.9}\ \mathrm{M}_\odot = (\sigma/128\ \mathrm{km/s})^{2.73} \sim (3\sigma/\sigma_\odot)^{2.73}$, we find that the system is unstable for masses $\geq 3.5 \times 10^8\ \mathrm{M}_\odot$.

Also, under the condition that the relaxation timescale is comparable to or shorter than t_H, Escala (2021) derived the following equation from equation 1.3.1,

$$R \leq \left(\frac{t_H \eta}{0.1} \ln\left(\frac{M}{\eta}\right)\right)^{2/3} \left(\frac{G}{M}\right)^{1/3}. \tag{1.4.3}$$

In Fig. 1.4.1 the black star represents the mass and radius of the black hole observed in M87 (Event Horizon Telescope Collaboration et al., 2019), which is the closest object to the black line that represents the Schwarzschild radius as a function of mass. The red circles are the effective radii and masses of NSCs (from early and late type galaxies), observed by Georgiev et al. (2016). The black and open circles are the masses and resolved radii ($R_{resol} = 0.5 d_{resol}$, d_{resol} is the spatial resolution of the observation) of possible MBHs, the black circles are the well-resolved MBHs, which show an influences radius (R_{inf}) three times larger than d_{resol} (i.e. $R_{inf} > 3d_{resol}$). The open circles are the unresolved MBHs ($R_{inf} < 3d_{resol}$), observations from Gültekin et al. (2009). We also represent the conditions of equations 1.4.1 and 1.4.3, as the solid blue line and the dashed green line, respectively, both for $t_H = 10^{10}$ yr. The intersection of both lines occurs at the value of the critical mass defined by equation 1.4.2 which is represented by the solid green line ($\sim 3.5 \times 10^8\ \mathrm{M}_\odot$, as described by Leigh et al. (2012)).

The left side of the solid blue line ($t_H < t_{coll}$) is the region where collisions dominate the cluster dynamics, while the right side ($t_H > t_{coll}$) represents the region where collisions are avoided. These collision timescales are relevant for

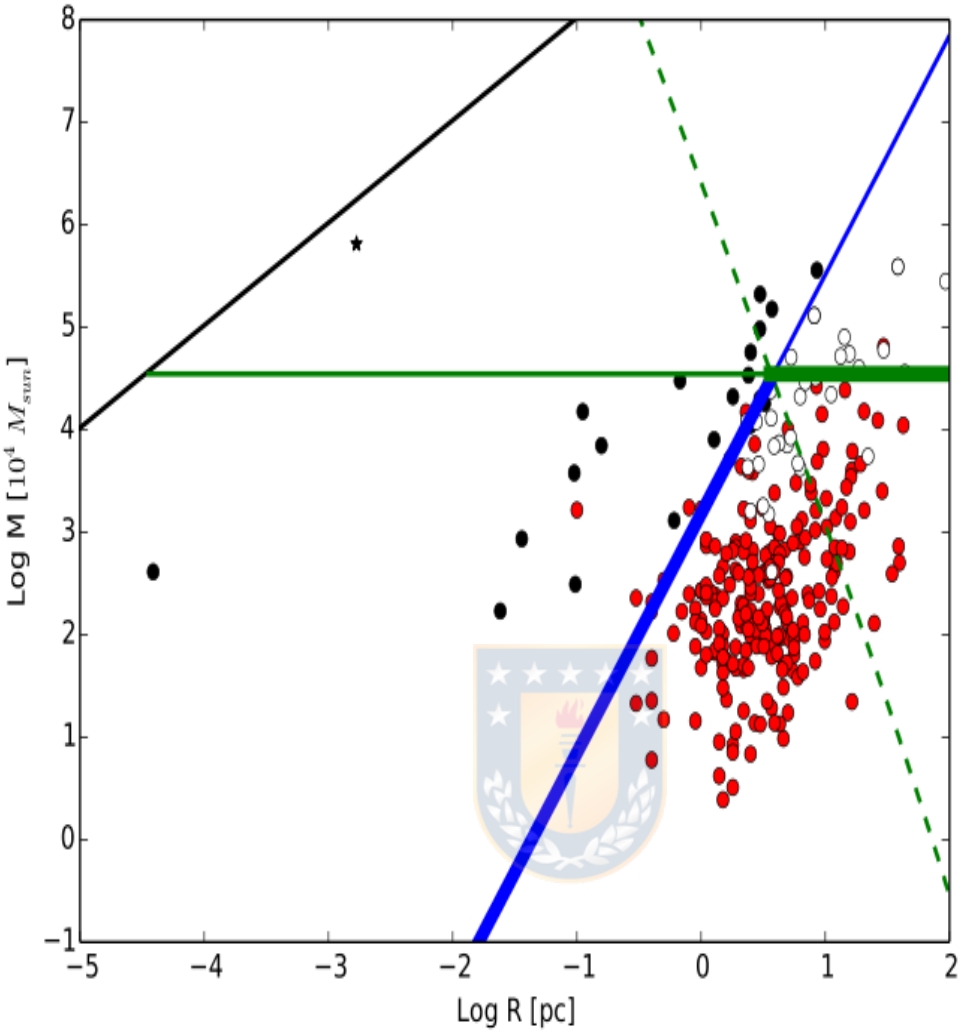

Figure 1.4.1: The black star is from the black hole shadow of M87 (Event Horizon Telescope Collaboration et al., 2019), the solid black line is the Schwarzschild radius as a function of mass. The red circles are the effective radii and masses of NSCs, the black circles are the well-resolved MBHs and the open circles are the unresolved MBHs. The solid blue, the dashed green and the solid green lines are from equations 1.4.1, 1.4.3, 1.4.2, respectively.

Source: Escala (2021).

the stability of the cluster against stellar collisions; in the core of the cluster the collisions occur more frequently, then the NSCs can coexist with an unstable core triggered by the Spitzer instability (Spitzer, 1969; Portegies Zwart and McMillan, 2002). The red points are on the right side of the solid blue line where the collisions are not relevant. It is very important to mention that the properties

represented by these red points are from current observations. The NSCs can have a radius approximately ten times smaller at the moment of formation (Banerjee and Kroupa, 2017). However, the evolution process must be considered, because the effective radius of the cluster expands (Baumgardt et al., 2018; Panamarev et al., 2019), moving the red dots from left to right. The cluster expansion is related to the relaxation timescale which is represented by the dashed green line which intersects the solid blue line at the same value of the solid green line, which comes from the condition of equation 1.4.2. All the NSCs are below this line where $t_{relax} \leq t_{coll}$. The absence of NSC above this line where $t_{relax} \geq t_{coll}$ can be explained since the cluster is not allowed to expand before the collisions start, so it is unstable under collisions (Escala, 2021). The black and white dots are distributed in two trends, the resolved MBHs are in the region where the collisions dominated the cluster dynamics, while the unresolved MBHs are in the same region as the NSCs. The positions of the white dots can be explained by the low resolution since their properties could include stellar effects within the radius of influence, so they can be considered as stellar systems (Escala, 2021).

1.5 The NSCs as a formation path of MBHs in Galactic Nuclei

The mass of the CMO can be easily determined as the sum of the mass of the nuclear stellar cluster and the black hole $M_{CMO} = M_{NSC} + M_{BH}$. With the black hole formation efficiency ϵ_{BH}, the mass of the BH must be $M_{BH} = \epsilon_{BH} M_{CMO}$ and the mass of the NSC is $M_{NSC} = (1 - \epsilon_{BH}) M_{CMO}$, therefore the efficiency is defined as:

$$\epsilon_{BH} = \left(1 + \frac{M_{NSC}}{M_{BH}}\right)^{-1}. \tag{1.5.1}$$

In Fig. 1.5.1, we display the observed black hole formation efficiency (ϵ_{BH}; black hole mass over total mass) as a function of the total mass of the CMO (M_{CMO}). The measurements from Neumayer et al. (2020) are represented by the black dots. Lower limits from observational data are denoted by the upper triangles ($\epsilon_{BH} \geq 0.9$ at $M_{CMO} \geq 3 \times 10^8$ $M_\odot$) and upper limits by the lower triangles ($\epsilon_{BH} \leq 0.15$ at $M_{CMO} \leq 3 \times 10^7$ $M_\odot$). There is a transition regime between

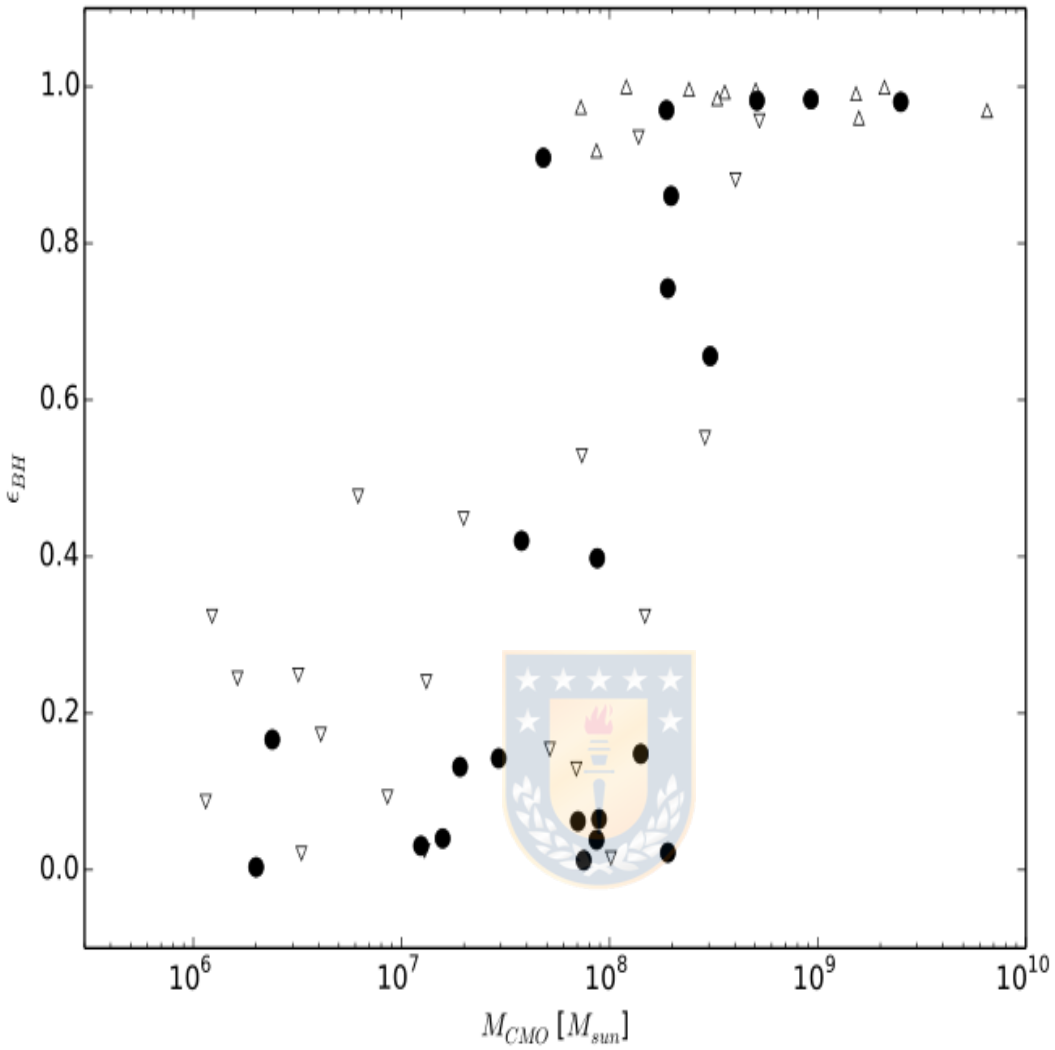

Figure 1.5.1: ϵ_{BH} is the observed black hole formation efficiency (black hole mass over total mass) as a function of the total mass of the CMO (M_{CMO}). The black dots are from Neumayer et al. (2020). The efficiency includes upper and lower limits, depending on the available observed quantities. The upper limit is denoted by the lower triangles ($\epsilon_{BH} \leq 0.15$ at $M_{CMO} \leq 3 \times 10^7$ $M_\odot$) and the lower limit is denoted by the upper triangles ($\epsilon_{BH} \geq 0.9$ at $M_{CMO} \geq 3 \times 10^8$ $M_\odot$).

Source: Escala (2021).

3×10^7 $M_\odot \leq M_{CMO} \leq 3 \times 10^8$ $M_\odot$ that shows a rapid increase of ϵ_{BH}. The trend of ϵ_{BH} agrees with the Fokker-Planck models of galactic nuclei developed by (Lee, 1987; Quinlan and Shapiro, 1990), which shows a transition called 'merger instability' in the formation of the CMO at masses over or similar to 10^7 $M_\odot$. Also the upper limit is in agreement with the condition given by Leigh et al. (2012).

Chapter 2

NBODY6++GPU

NBODY6++GPU is a direct high precision N-body simulation code based on the N-body code NBODY6 (Aarseth, 2000) and the parallel multi-node code NBODY6++ (Spurzem, 1999). This code uses the Hermite 4^{th} order integrator scheme developed by Makino (1991), which improves on the previous standard scheme developed by Aarseth (1985), which has trouble solving higher-order integrators. It also includes a spatial hierarchy to speed up computational calculations, there is a list of neighbor particles which is divided into two lists, the regular force and the irregular force, which are related to the distance of the neighbor from the particle (Ahmad and Cohen, 1973). It also contains an algorithm to regulate close encounters, binaries (Kustaanheimo and Stiefel, 1965) and multiple systems (Mikkola and Aarseth, 1990, 1993). Shared memory parallelization was developed by Nitadori and Aarseth (2012). Gravitational forces between particles are calculated in Graphics Processing Units (GPUs) (Wang et al., 2015); this GPU implementation improves to overall computing performance, especially for gravitational forces of long range (Nitadori and Aarseth, 2012; Wang et al., 2015, 2016).

2.1 The Hermite Integration scheme

The particles are fully described by their mass m, position $\mathbf{r}_0$ and velocity $\mathbf{v}_0$ at the initial time t_0. The motion of a particle i can be described by the equation of momentary acceleration $\mathbf{a}_{0,i}$ with respect to all other particles and its time derivative $\dot{\mathbf{a}}_{0,i}$ as

$$\mathbf{a}_{0,i} = -\sum_{i \neq j} G m_j \frac{\mathbf{R}}{R^3}, \tag{2.1.1}$$

$$\dot{\mathbf{a}}_{0,i} = -\sum_{i \neq j} G m_j \left[\frac{\mathbf{V}}{R^3} + \frac{3\mathbf{R}(\mathbf{V}\cdot\mathbf{R})}{R^5} \right], \tag{2.1.2}$$

where $\mathbf{R}$=$\mathbf{r}_{0,i}$-$\mathbf{r}_{0,j}$ is the relative coordinate, R=$|\mathbf{r}_{0,i}$-$\mathbf{r}_{0,j}|$ the modulus, $\mathbf{V}$=$\mathbf{v}_{0,i}$-$\mathbf{v}_{0,j}$ the relative velocity with respect to the particle j and G is the gravitational constant.

The Hermite method follows the motion of the particle, using a Taylor series to predict the new position $\mathbf{r}_p$ and velocity $\mathbf{v}_p$ at the next time step t:

$$\mathbf{r}_{p,i}(t) = \mathbf{r}_0 + \mathbf{v}_0(t - t_0) + \mathbf{a}_{0,i}\frac{(t - t_0)^2}{2} + \dot{\mathbf{a}}_{0,i}\frac{(t - t_0)^3}{6}, \tag{2.1.3}$$

$$\mathbf{v}_{p,i}(t) = \mathbf{v}_0 + \mathbf{a}_{0,i}(t - t_0) + \dot{\mathbf{a}}_{0,i}\frac{(t - t_0)^2}{2}. \tag{2.1.4}$$

Hermite interpolation allows an approximation of the terms of higher acceleration by another Taylor series:

$$\mathbf{a}_i(t) = \mathbf{a}_{0,i} + \dot{\mathbf{a}}_{0,i} \cdot (t - t_0) + \frac{\mathbf{a}^{(2)}_{0,i} \cdot (t - t_0)^2}{2} + \frac{\mathbf{a}^{(3)}_{0,i} \cdot (t - t_0)^3}{6}, \tag{2.1.5}$$

$$\dot{\mathbf{a}}_i(t) = \dot{\mathbf{a}}_{0,i} + \dot{\mathbf{a}}^{(2)}_{0,i} \cdot (t - t_0) + \frac{\mathbf{a}^{(3)}_{0,i} \cdot (t - t_0)^2}{2}. \tag{2.1.6}$$

The values of $\mathbf{a}_{p,i}$ and $\dot{\mathbf{a}}_{p,i}$ can be calculated with equations 2.1.1 and 2.1.2 using the predicted values of $\mathbf{r}_{p,i}$ and $\mathbf{v}_{p,i}$ that come from equations 2.1.3 and 2.1.4. Once $\mathbf{a}_{p,i}$ and $\dot{\mathbf{a}}_{p,i}$ are calculated and replaced in equation 2.1.5 it is possible to show that

$$\mathbf{a}^{(3)}_{0,i} = 12\frac{\mathbf{a}_{0,i} - \mathbf{a}_{p,i}}{(t_{t0})^3} + 6\frac{\dot{\mathbf{a}}_{0,i} - \dot{\mathbf{a}}_{p,i}}{(t_{t0})^2}, \tag{2.1.7}$$

$$\mathbf{a}_{0,i}^{(2)} = -6\frac{\mathbf{a}_{0,i} - \mathbf{a}_{p,i}}{(t_{t0})^2} - 2\frac{2\dot{\mathbf{a}}_{0,i} - \dot{\mathbf{a}}_{p,i}}{t_{t0}}. \tag{2.1.8}$$

Then if equations 2.1.3 and 2.1.4 are expanded by two orders more, it is possible to write the position $\mathbf{r}_{1,i}$ and velocity $\mathbf{v}_{1,i}$ of the particle i at the computation time t_1 as

$$\mathbf{r}_{1,i}(t) = \mathbf{r}_{p,i}(t) + \frac{\mathbf{a}_{0,i}^{(2)}(t - t_0)^4}{24} + \frac{\mathbf{a}_{0,i}^{(3)}(t - t_0)^5}{120}, \tag{2.1.9}$$

$$\mathbf{v}_{1,i}(t) = \mathbf{v}_{p,i}(t) + \frac{\mathbf{a}_{0,i}^{(2)}(t - t_0)^3}{6} + \frac{\mathbf{a}_{0,i}^{(3)}(t - t_0)^4}{24}. \tag{2.1.10}$$

The local error of r and v between two time steps $\Delta t = t_1 - t_0$ must be of the order of $\vartheta(\Delta t^5)$ while the global error for a fixed physical time integration must be of the order of $\vartheta(\Delta t^4)$ (Makino, 1991).

2.2 Individual and block time steps

Stellar systems are complex environments that include several processes with different time scales such as the orbital periods of binary systems that are of the order of a few days, while the relaxation time scale of a star cluster can reach values of millions or even billions of years. Due to this, it is necessary to use different time steps to characterize the evolution of a particle as a function of the fluctuations that act on it. Aarseth (1963) developed the 'individual time step scheme', the main idea of which is to use small time step integration for particles in regions where force changes are relatively large, while large time step integration is used for particles in regions of slowly changing relative forces.

Each particle has its own time step Δt_i, called a 'block time step'. In Fig. 2.2.1 the particle i has the smallest time step, therefore its phase space coordinates are determined at each time step. The time step of the particle k is twice the time step of the particle i and its coordinates are determined as an extrapolation in the odd time steps. The particle l has a time step $\Delta t_l = 4\Delta t_i$. The dotted line represents a full force calculation; the step width can be altered after a full force calculation as shown in Fig. 2.2.1 after the 8 time steps where the particle k time

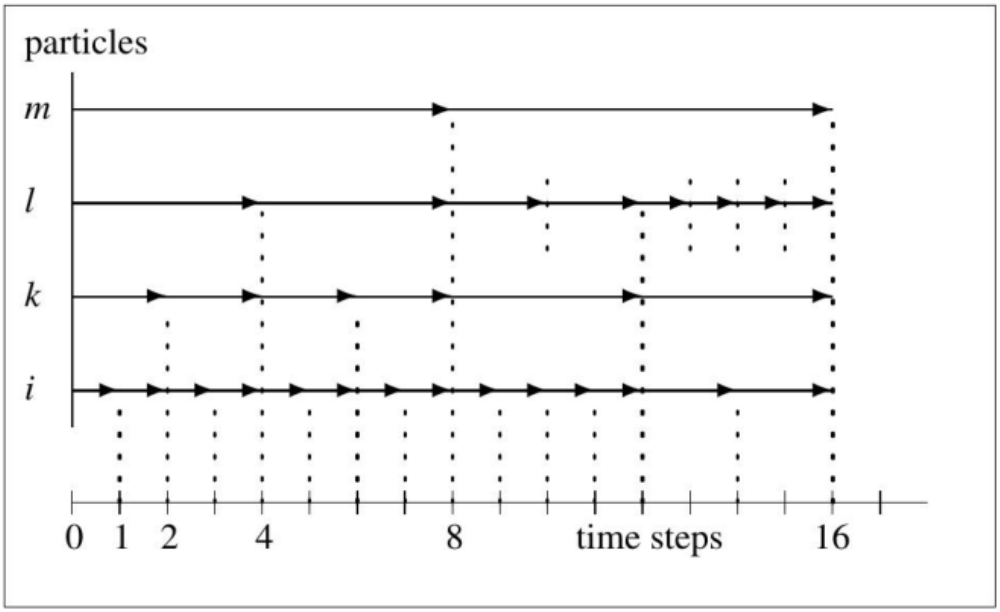

Figure 2.2.1: Example of block time steps for four particles.

Source: Khalisi et al. (2019).

step is doubled. The time step has to be commensurate with the time step of each particle and the total time to guarantee a hierarchy.

A first estimation of the particle time step comes from the rate of change of acceleration $\Delta t_i \propto \sqrt{\mathbf{a}_i/\dot{\mathbf{a}}_i}$, Aarseth (1985) after some experimentation developed the following formula

$$\Delta t_i = \sqrt{\eta \frac{|\mathbf{a}_{1,i}||\mathbf{a}^{(2)}_{1,i}| + |\dot{\mathbf{a}}_{1,i}|^2}{|\dot{\mathbf{a}}_{1,i}||\mathbf{a}^{(3)}_{1,i}| + |\mathbf{a}^{(2)}_{1,i}|^2}}, \tag{2.2.1}$$

where η is a dimensionless accuracy parameter to control the error and usually takes values between $0.001 - 0.002$.

2.3 The Ahmad-Cohen method

Calculating the positions and velocities of each particle due to the contribution of all the other particles is time-consuming, especially if the simulation include a large number of particles. To speed up the calculations, Ahmad and Cohen

(1973) developed a method whose main idea is to use a list of neighbors of each particle, where the list is divided into two parts, the first for the integration of regular forces for large time steps and the second for the integration of irregular forces for small steps of time, so that:

$$\mathbf{a}_i = \mathbf{a}_{i,reg} + \mathbf{a}_{i,irr}. \tag{2.3.1}$$

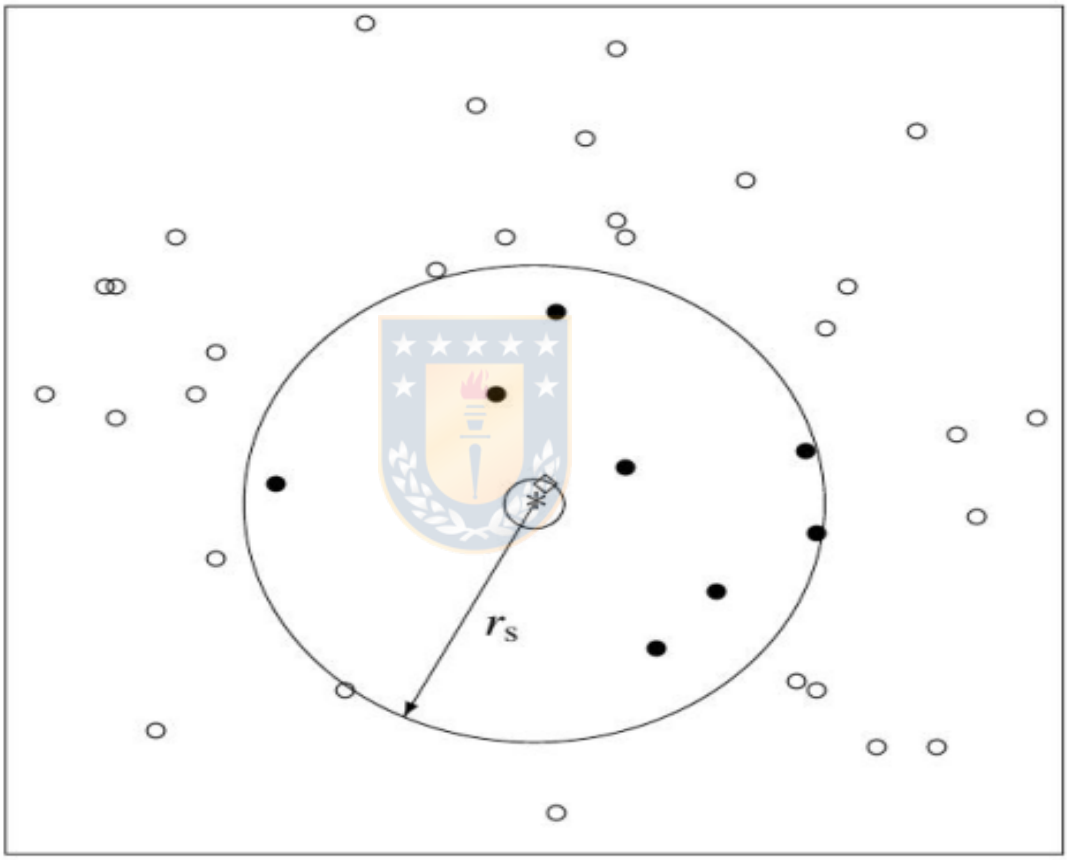

Figure 2.3.1: A particle with its neighbour radius r_s. Empty dots are particles outside of r_s and black dots are particles inside r_s.

Source: Khalisi et al. (2019).

Whether a particle is a neighbor or not is determined by their distance, all members within the 'neighbors sphere' with radius r_s are on the irregular list, and the rest of the particles outside are on the regular list. The contribution of the irregular force is for particles that are close to the particle i. Since these particles are close to i, they must produce stronger fluctuations due to the gravitational force, therefore these integration must be carried out more frequently than the integration of

the regular force from particles that are more distant from i since their position relative to i will not have large changes.

2.4 KS-Regularization

The treatment of close encounters and binary systems in a star cluster is very expensive due to the small distances and therefore the small time steps involved in the stellar dynamics. Close encounters of stars reach a distance of the order of 10^{-6} pc with an associate timescale of 10^{-7} yr, while the evolution of star clusters is followed up to several Myr. Hence, if the star cluster contains a large number of binary systems, it becomes extremely expensive. To deal with a precise solution to this problem, Kustaanheimo and Stiefel (1965) developed an algorithm (KS-regularization) to treat close encounters and binary systems. Mikkola and Aarseth (1990, 1993) included chain regularization to deal with multiple systems. All of these interactions play an important role in the dynamical evolution of star cluster. These interactions require very small time steps during the integration and can produce large errors with standard integrators such as the Hermite scheme, while truncation errors are avoided with KS-regularization. This algorithm replaces two close bodies with a center of mass particle and integrates them separately in a new coordinate system. Furthermore, in this new coordinate system, a harmonic oscillator accurately describes the close encounter of two bodies in the absence of disturbance.

2.5 GPU parallelization

For several decades, calculations of N-body interactions have challenged technology and astronomers, as direct force calculations follow an N^2 number of calculations, which provides a limit to expanding the number of particles. The graphics processing units (GPUs) together with the CUDA programming language are useful to speed up the N-body codes (Nitadori and Aarseth, 2012).

There is a subroutine called INTGRT that drives the numerical integration of the Ahmad-Cohen scheme using two libraries, one for the regular force and the second one for the irregular forces, called GPUNB and GPUIRR, respectively.

It is useful to distinguish between the attracting particles called j-particles and

the attracted ones called i-particles. The GPUNB library calculates the regular forces and generates neighbor lists for a determined set of particles with unique or multiple threads of GPU(s). Each i-particle is assigned to each GPU thread. Position, velocity, force, neighbor radius, time derivative, and neighbor particle count are kept in the record of each thread. On the other hand, the predicted mass, position, and velocity of j-particles are transmitted from memory to all threads, and the forces on multiple particles i are evaluated in parallel. If particle j happens to be a neighbor of i, the index j is written to the neighbor list in the memory. Therefore the predicted mass, position, and velocity of the j-particles are sent from the host, then the regular force and neighbor list of i-particles are calculated, so both are evaluated in a single call. The GPUIRR library was named so as its main purpose is to speed up irregular force calculations using GPUs. However, the GPU implementation was slower than the CPU code with SSE/AVX and OpenMP. GPUIRR computes many internal states including position, velocity, acceleration. Mass and time of the last integration of the i-particle are used to obtain the prediction. After each irregular step these quantities are recalculated, besides the neighbor list of i-particles are saved for the calculation of the irregular force, the list is saved after each regular step. The library receives a list of irregular particles and returns the irregular force. The GPUIRR library is synchronized with the multicore CPU and SIMD parallelism such as the Streaming SIMD Extensions (SSE) and Advanced Vector Extensions (AVX). The use of openMP parallelization for i-particles is simple. The SIMD parallelism is used to compute the j-parallelism for a single i-particle. SSE is used to compute the pairwise forces of an i-particle from multiple four-way j-particles, and, AVX is used to compute the pairwise forces of an i-particle from multiple eight-way j-particles, is necessary to select them from non-contiguous addresses displayed in the list of neighbors (Nitadori and Aarseth, 2012).

Fig. 2.5.1 shows a single simulation cycle. The integration can be divided into three hierarchical parts from the smallest to the largest time steps: the KS regularization (KS), the irregular force (Irr.), and the regular force (Reg.). After every regular step occurs one 'Adjust', which is parallelized by multiple GPUs, the irregular forces are parallelized by AVX/SSE with OpenMP, and KS-regularization is solved by a simple CPU.

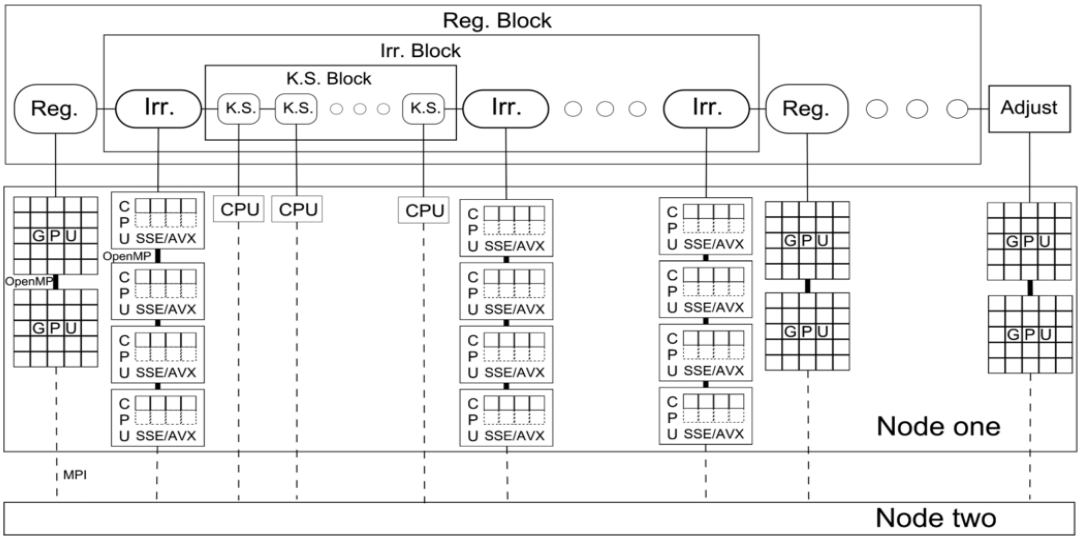

Figure 2.5.1: Example of a one cycle simulation with the code NBODY6++GPU.

Source: Wang et al. (2015).

2.6 Input File of NBODY6++GPU

Here I describe the template of a regular input file of NBODY6++GPU:

```
KSTART TCOMP TCRITp isernb iserreg iserks
N NFIX NCRIT NRAND NNBOPT NRUN NCOMM
ETAI ETAR RS0 DTADJ DELTAT TCRIT QE RBAR ZMBAR
KZ(1) KZ(2) KZ(3) KZ(4) KZ(5) KZ(6) KZ(7) KZ(8) KZ(9) KZ(10)
KZ(11) KZ(12) KZ(13) KZ(14) KZ(15) KZ(16) KZ(17) KZ(18) KZ(19) KZ(20)
KZ(21) KZ(22) KZ(23) KZ(24) KZ(25) KZ(26) KZ(27) KZ(28) KZ(29) KZ(30)
KZ(31) KZ(32) KZ(33) KZ(34) KZ(35) KZ(36) KZ(37) KZ(38) KZ(39) KZ(40)
KZ(41) KZ(42) KZ(43) KZ(44) KZ(45) KZ(46) KZ(47) KZ(48) KZ(49) KZ(50)
DTMIN RMIN ETAU ECLOSE GMIN GMAXX SMAX
ALPAH BODY1 BODYN KBIN0 NHI0 ZMET EPOCH0 DTPLOT
Q VXROT VZROT RTIDE
```

N is the number of objects, NNBPOT is the optimal neighbour number, NRAND is the random number to initialize the position of the particles, RBAR is the virial radius in pc, ZMBAR is the mean mass in solar units, BODY1 and BODYN are the maximum and minimum particle mass, respectively. These are the parameters that we vary, the rest of parameters are chosen according to the manual of

NBODY6++GPU.

```
1 1000000.0 1.E6 40 40 0
10000 1 10 465 170 1 10
0.01 0.01 0.3 1.0 1.0 200000.0 2.0E01 0.01 10.0
0 1 1 0 1 0 4 0 1 2
0 1 0 0 0 0 0 4 3 0
1 1 2 0 0 2 -1 0 0 2
1 0 2 0 0 0 1 1 0 0
0 0 0 0 0 4 -2 0 1 0
1.0E-03 1.0E-03 0.1 1.0 1.0E-06 0.001 1
1.0 10.0 10.0 0 0 0.0001 0 1.0
0.5 0.0 0.0 0.0
```

2.7 Initial conditions

We are testing the new scenario of SMBH formation in NSCs proposed by Escala (2021) using a spherical distribution of stars from the Plummer (1911) model.

We evolved the clusters for 1 Myr and 10 Myr, varying the initial number of stars as $N = 5 \times 10^2, 10^3, 10^4$. We use equal-mass stars, the mass of each star (M_*) can take values of 10 or 50 $M_\odot$ with an associated initial stellar radius $R_* = 4.7, 11.7$ $R_\odot$, respectively. The mass-radius relation is based on Bond et al. (1984) and Demircan and Kahraman (1991) and given as:

$$\frac{R_*}{R_\odot} = 1.6 \times \left(\frac{M_*}{M_\odot}\right)^{0.47}, 10\ M_\odot \leq M_* < 50\ M_\odot, \tag{2.7.1}$$

$$\frac{R_*}{R_\odot} = 0.85 \times \left(\frac{M_*}{M_\odot}\right)^{0.67}, 50\ M_\odot \leq M_*. \tag{2.7.2}$$

We simulated 9 nuclear stellar clusters, covering different regions of the parameters space as described in section 1.4. Fig.2.7.1 and Fig.2.7.2 shows the curves at the value of t_H equal to 1Myr and 10 Myr, respectively.

A summary of our initial conditions is shown in Table 2.7.1.

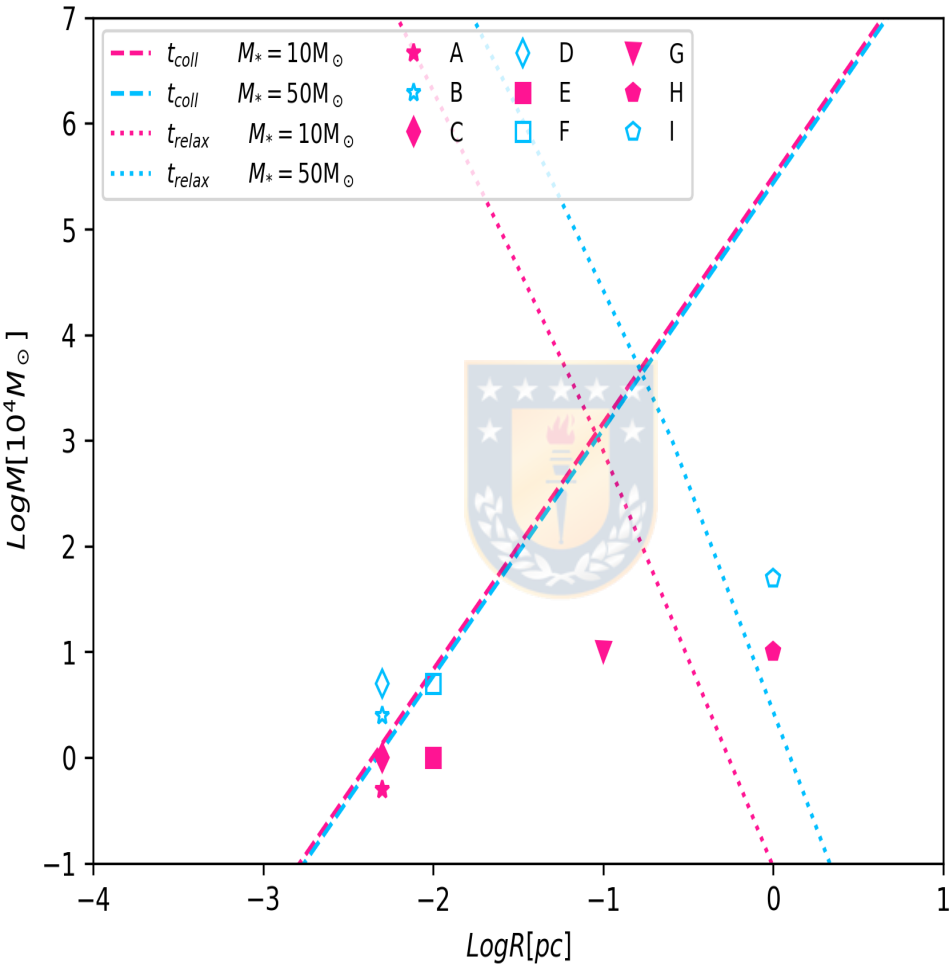

Figure 2.7.1: The magenta and cyan symbols are for $M_* = 10, 50$ $M_\odot$ respectively. The dashed lines are from the condition of equation 1.4.1, while the dotted lines are from equation 1.4.3 both for a time evolution of 1 Myr.

Source: Vergara et. al. in prep.

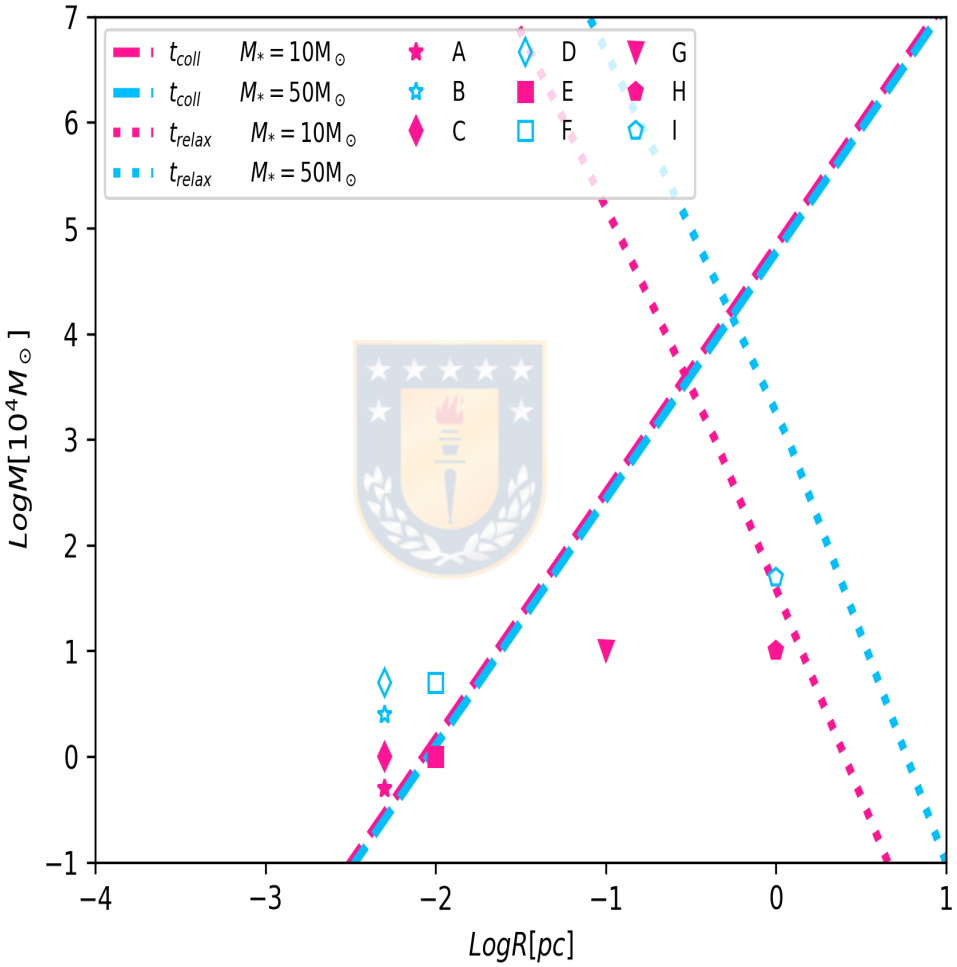

Figure 2.7.2: The magenta and cyan symbols are the same as Fig. 2.7.1. The dashed and dotted lines are for a time evolution of 10 Myr.

Source: Vergara et. al. in prep.

Table 2.7.1: The virial radius is R_v, M_{ini} is the initial mass of the cluster, N is the initial number of stars, the stellar mass and radius is M_* and R_* respectively.

Models	R_v[pc]	M_{ini}[$M_\odot$]	N	M_*[$M_\odot$]	R_*[$R_\odot$]
A	5×10^{-3}	$5{\times}10^3$	5×10^2	10	4.7
B	5×10^{-3}	$25{\times}10^3$	5×10^2	50	11.7
C	5×10^{-3}	10^4	10^3	10	4.7
D	5×10^{-3}	$5{\times}10^4$	10^3	50	11.7
E	10^{-2}	10^4	10^3	10	4.7
F	10^{-2}	$5{\times}10^4$	10^3	50	11.7
G	10^{-1}	10^5	10^4	10	4.7
H	1	10^5	10^4	10	4.7
I	1	$5{\times}10^5$	10^4	50	11.7

Chapter 3

Results

In this chapter, we summarize our main results showing first a description of the evolution of our models, followed by an analysis of the black hole formation efficiency ϵ_{BH}, obtained from the simulations.

3.1 Nuclear star cluster evolution

In this section, we analyze the time evolution of two models B and G. Model B has $M_{ini} = 5 \times 10^4$ $M_\odot$, with a viral radius of 0.005 pc. Model G has an initial mass of 10^5 $M_\odot$, with $R_v = 1$ pc. Model B is in the region where collisions dominate the stellar dynamics (i.e. $t_{coll} < t_{relax}$). Model G is in the region where collisions are avoided (i.e. $t_{coll} > t_{relax}$). We present the cumulative mass of escapers normalized by the initial mass M_{ini}, the number of collisions normalized by the initial number of stars N, the black hole formation efficiency ϵ_{BH} described by equation 1.5.1 and the Lagrangian radii corresponding to 90%, 50%, and 10% of the enclosed mass.

In Fig. 3.1.1 we show the evolution of model B over 1 Myr. The top panel shows the cumulative mass of stars escaping from the cluster normalized by the initial mass M_{ini}; the stellar cluster loses around 42% of the initial mass after 1 Myr. The first middle panel shows the total number of collisions N_{coll} normalized by the initial number of stars $N = 500$; after 1 Myr more than 80 collisions have occurred. The second middle panel shows the black hole formation efficiency $_{BH}$ described in section 1.4, ϵ_{BH} reaches a value of around 28%. The stellar system forms a

single massive object of 4150 $M_\odot$. The bottom panel shows the Lagrangian radii at 90%, 50%, and 10% of the enclosed mass. The outer zone of the stellar system corresponding to 90% of the mass shows an expansion until around 0.1 Myr, then remains almost constant. The middle zone (i.e 50%) shows a smooth expansion all the time while the inner zone at 10% of the enclosed mass shows a decrease at the beginning of the simulation.

In Fig. 3.1.2 we display the evolution of the same model B over 10 Myr. The panels are the same as in Fig. 3.1.1. The top panel shows that around 58% of the initial mass is lost. The first middle panel shows that around 83 collisions in total occurred, most collisions happened in the first Myr. The most massive object reaches a mass of 4300 $M_\odot$. The second middle panel shows that the black hole formation efficiency increases until a value of 41%. After 2 Myr, the 90% and 50% Lagrangian radii curves start to overlap because there is so much mass loss. The 10% Lagrangian radius shows a rapid decrease at first followed by an expansion and then remains almost constant.

Comparing Fig. 3.1.1 and Fig. 3.1.2, after 9 Myr, the cumulative mass of stars escaping from the star system increases by 16%. The number of collisions increases only a bit meaning that the most massive object reaches a mass of 4300 $M_\odot$. The black hole formation efficiency $_{BH}$ increases by 13%; this increase is more due to the escapers than the collisions since the mass of the most massive object increases only by 150 $M_\odot$ while there are several stars that escape from the stellar system.

Model B is one of the densest models. This model is very chaotic, showing a core contraction at the beginning. Almost all collisions occur in 1 Myr; there are also several escapers during this time, therefore the black hole formation efficiency also increases due to both processes. After 1 Myr only a few collisions occur, while the number of escapers continues to increase. This means that during the late times the increase of ϵ_{BH} is dominated more by the number of escapers than by stellar collisions. It may explain that in some of the observed systems a star cluster is no longer visible.

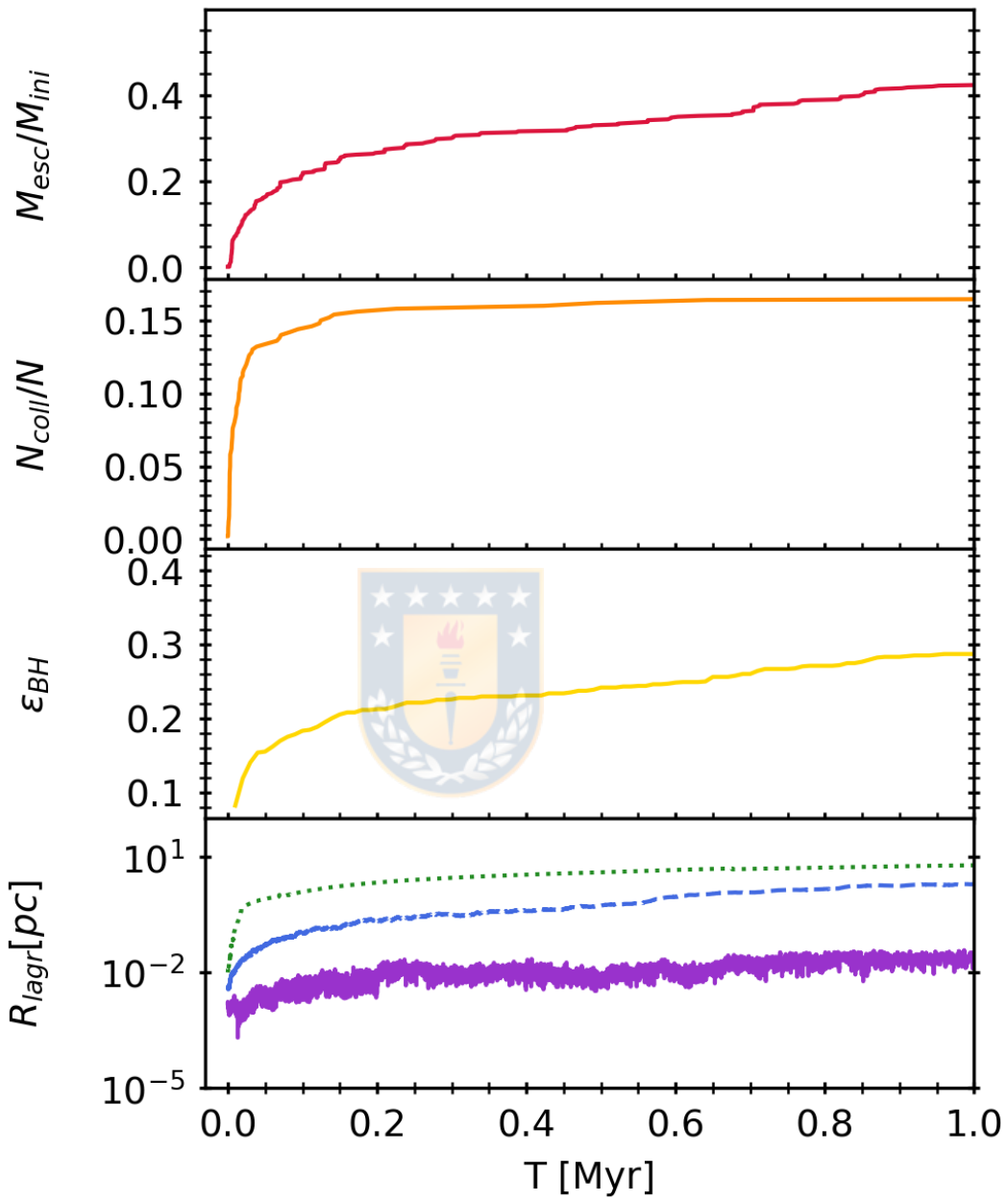

Figure 3.1.1: Evolution of model B for 1 Myr. Top panel: The cumulative mass of escapers normalized by the intial mass M_{ini}. First middle panel: The number of collisions normalized by the initial number of stars N. Second middle panel: The black hole formation efficiency ϵ_{BH} described by equation 1.5.1. Bottom panel: Lagrangian radii for the 10%, 50%, and 90% of the enclosed mass.

Source: Vergara et. al. in prep.

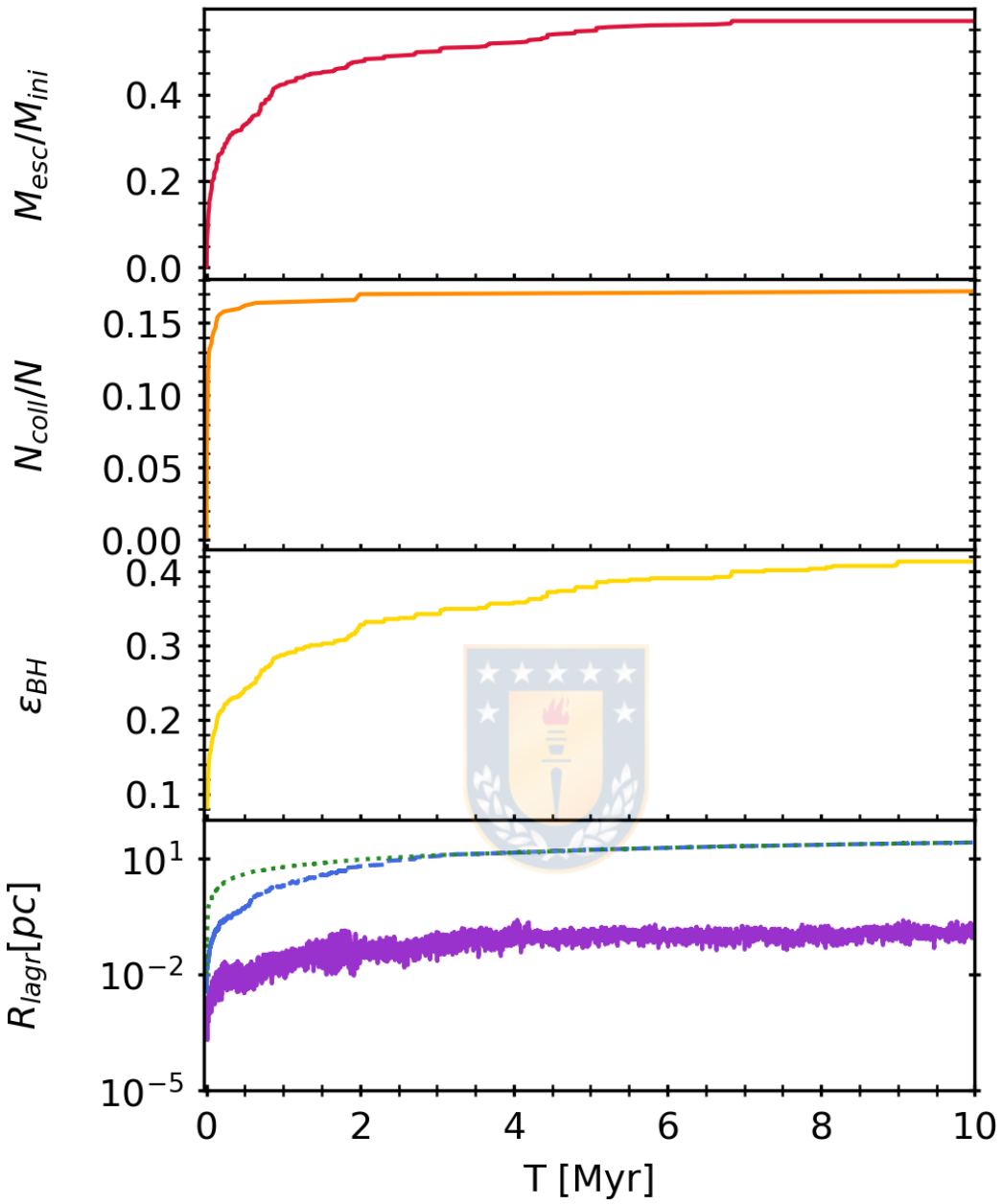

Figure 3.1.2: Evolution of model B for 10 Myr . Top panel: The cumulative mass of escapers normalized by the intial mass M_{ini}. Panels are the same as in Fig. 3.1.1.

Source: Vergara et. al. in prep.

Fig. 3.1.3 shows the evolution of model G over 3 Myr. The panels are the same as in Fig. 3.1.1. The top panel shows that after 3 Myr 220 stars of 10 $M_\odot$ have escaped from the cluster. The first middle panel shows that around 140 collisions occurred during this time. The second middle panel shows that the black hole formation efficiency is very low; after 3 Myr it reaches a value of less than 2%. The most massive object reaches a mass of 1670 $M_\odot$. The Lagrangian radii at 90% and 50% remain almost constant, while the Lagrangian radii at 10% shows a smooth decrease until 2.5 Myr when the core contraction occurs, followed by an expansion. After 2.5 Myr there is an increase in the number of escapers from the system. An increase in the number of collisions also occurs, several of them with the most massive object, and the black hole formation efficiency also increases after 2.5 Myr.

We show the evolution of this model until 3 Myr, since until 1 Myr, the number of collisions and escapers is very low, so it is not quite interesting. Model G has a long relaxation time ($t_{relax} \approx 16260$ Myr), so it takes longer for core-collapse to occur.

Fig. 3.1.4 shows the evolution of model G over 10 Myr. The panels are the same as in Fig. 3.1.1. The top panel shows that around 8% of the stellar mass is lost due to the escapers. The first middle panel shows around 700 stellar collisions. The most massive object reaches a mass of 6700 $M_\odot$. The second middle panel shows that the black hole formation efficiency reaches a value of 7%. The Lagrangian radius at 90% shows an expansion over time, the Lagrangian radius at 50% remains almost constant while the Lagrangian radius at 10% shows a decrease until 2.5 Myr, followed by an expansion and then remains almost constant.

Comparing Fig 3.1.3 and Fig 3.1.4, after 9 Myr, more than 600 stars have escaped from the cluster. The most massive object increases its mass to more than 5000 $M_\odot$. The black hole formation efficiency increases by 5%. Until 2.5 Myr, the system is still very stable so there are very few stellar collisions and escapers. The stellar system goes through core contraction after 2.5 Myr, therefore the largest increase of the most massive object in mass through stellar collisions occurs after this time.

Model G lost only a small fraction of its initial mass due to the stars that escape from the system, around 8%. This stellar system shows few collisions before 2.5 Myr, forming a massive object of 1670 $M_\odot$. At this time there is a small core

contraction, so after 2.5 Myr the number of collisions increases and several of them occur with the most massive object which increases in mass, reaching a mass of 6700 M $_{++}$ yet this star system shows a black hole formation efficiency of only 8% after 10 Myr.

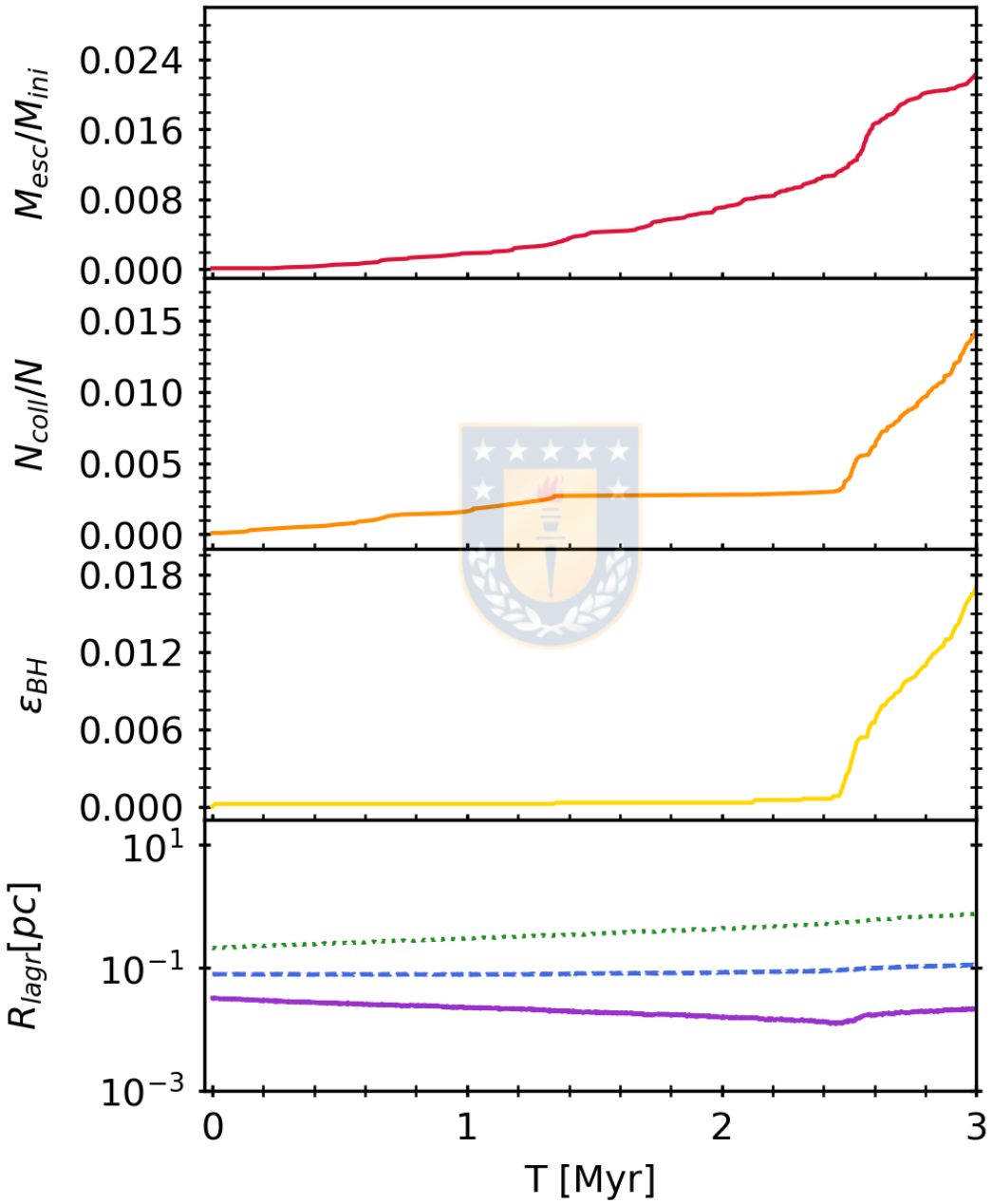

Figure 3.1.3: Evolution of model G for 1 Myr. Panels are the same as in Fig. 3.1.1.

Source: Vergara et. al. in prep.

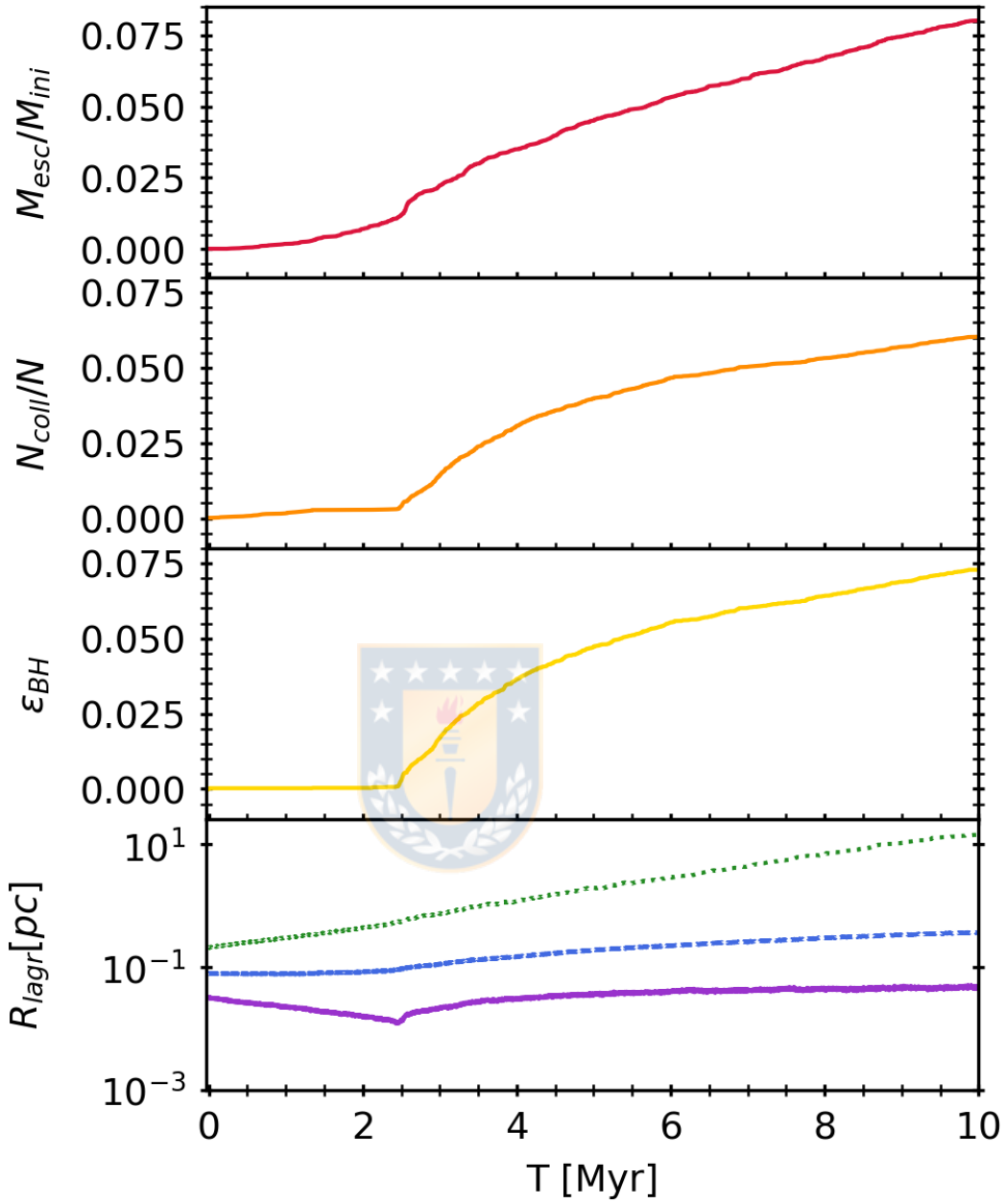

Figure 3.1.4: Evolution of model G for 10 Myr . Panels are the same as in Fig. 3.1.1.

Source: Vergara et. al. in prep.

Stellar gravitational interactions can cause stars to be ejected from the cluster, taking kinetic energy with them and causing the cluster energy to redistribute, leading the cluster to undergo core contraction. This collapse of the stellar system is related to the formation of the most massive object since the stars are more likely to collide with each other, therefore there is an increase in the number of collisions. At the same time many of these collisions occur with a single object.

Model G is more massive than Model B, but also has a larger virial radius, forming a more massive object than model B; nonetheless, its evolution is less chaotic because the collision time scale of model B is shorter than the relaxation time scale, while model G has a relaxation time scale larger than the collision time scale. This can be observed in Fig.2.7.1, since the models are in a different part of the parameters space; model B is in a region where the collisions dominate the stellar dynamics, while model G is in a region where stellar collisions are scarce. Also, the chaotic gravitational interaction of model B shows a larger fraction of initial mass loss due to stellar escapers than model G. This means that model B has a higher black hole formation efficiency than the model G, while nonetheless model G forms a more massive object than model B.

3.2 Black hole formation efficiency

The following results are based on the average of three simulations for the same single configuration with a different random seed to obtain reliable statistics and error estimates.

We define the critical mass (M_{crit}), which is the mass at which the virial radius of our clusters crosses the collision line in Fig. 2.7.1. We use this mass to normalize the masses of the central massive objects. This mass is derived from equation 1.4.1 from (Escala, 2021):

$$M_{crit} = R^{7/3} \left(\frac{4\eta}{300 \xi^2 t_H G^{1/2}} \right), \tag{3.2.1}$$

where R is the virial radius, η and ξ are the stellar mass and radius, respectively, G is the gravitational constant and t_H is the simulation time.

In Fig 3.2.1, we display the black hole formation efficiency as a function of the initial mass of the nuclear cluster normalized by M_{crit} until 1 Myr. Model A shows a black hole formation efficiency of 18%. Model B has the same radius as model A, but has more massive stars. Therefore it has a higher mass density than model A. It shows a black hole formation efficiency of 25%. Model C has $\epsilon_{BH} = 24\%$. Model D is denser than model C and shows the highest black hole formation efficiency of 37%. Models E and F have $\epsilon_{BH} = 13\%$ and $\epsilon_{BH} = 23\%$, respectively. Model G has a very low ϵ_{BH} of less than 1%. Models I and H have the same black hole formation efficiency of 0. The systems are collisionless, so there is no massive object.

We summarize our results after 1 Myr in Table 3.2.1. We provide in the first column the model ID, in the second column the cummulative mass of the escapers (M_{esc}), in the third column the final black hole mass (M_{BH}), in the fourth column the mass final of the nuclear star cluster (M_{NSC}), in the fifth column the final mass of the central massive object (M_{CMO}) and the black hole formation efficiency (ϵ_{BH}) is in the last column. Note that the final masses are measured until 1 Myr.

Note that the masses of the stellar systems are related as follows:

$$M_{ini} = M_{CMO} + M_{esc} = M_{NSC} + M_{BH} + M_{esc}. \tag{3.2.2}$$

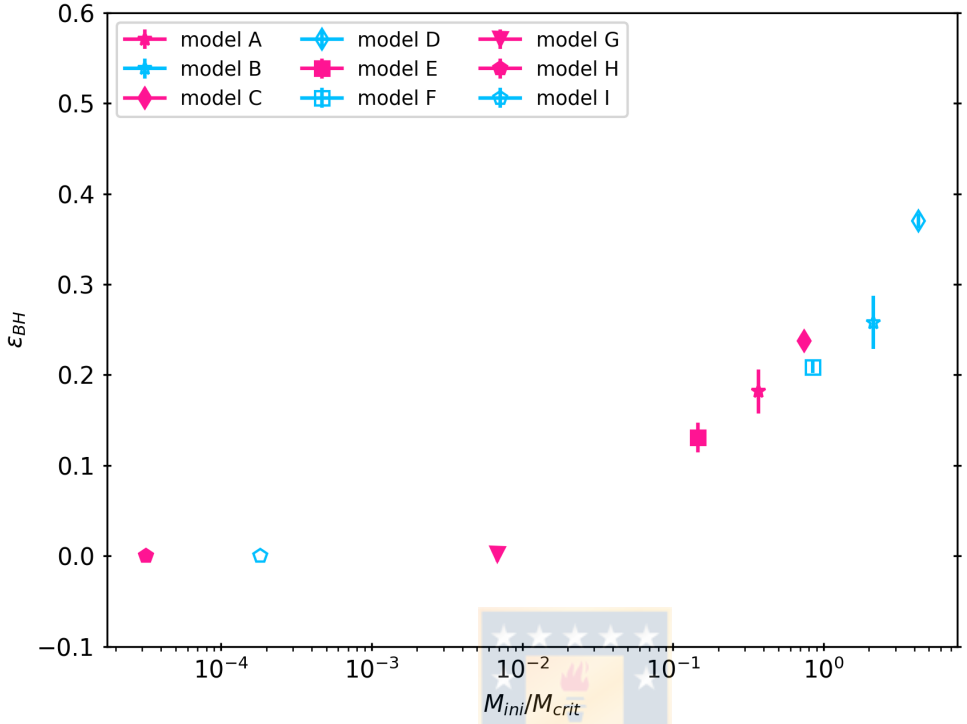

Figure 3.2.1: Black hole efficiency described by equation 1.5.1 against the initial mass of the nuclear star cluster normalized by the critical mass after 1 Myr.

Source: Vergara et. al. in prep.

Table 3.2.1: M_{esc} is the cummulative mass of the escapers, the final black hole mass is M_{BH}, M_{NSC} is the final mass of the nuclear star cluster, M_{CMO} is the sum of M_{BH} and M_{NSC}, and the black hole formation efficiency is ϵ_{BH}, all quantities are measured until 1 Myr.

Models ID	M_{esc} [$M_\odot$]	M_{BH} [$M_\odot$]	M_{NSC} [$M_\odot$]	M_{CMO} [$M_\odot$]	ϵ_{BH}
A	1743 ± 213	587 ± 47	2670 ± 254	3257 ± 213	$18 \pm 0.2\%$
B	10450 ± 414	3650 ± 356	10900 ± 561	14550 ± 414	$25 \pm 0.3\%$
C	3327 ± 9	1583 ± 19	5090 ± 28	6673 ± 9	$24 \pm 0.0\%$
D	22875 ± 1175	9900 ± 150	17225 ± 1025	27125 ± 1175	$37 \pm 0.1\%$
E	2350 ± 37	1000 ± 122	6650 ± 159	7650 ± 37	$13 \pm 0.2\%$
F	16817 ± 425	7517 ± 691	25667 ± 1077	33183 ± 425	$23 \pm 0.2\%$
G	187 ± 17	20	99793 ± 17	99800 ± 17	$0.02 \pm 0.0\%$
H	0	0	100000	100000	0%
I	0	0	100000	100000	0%

In Fig 3.2.2, we display the black hole formation efficiency against the mass of

the initial mass of the nuclear cluster normalized by the critical mass (M_{crit}) at 10 Myr. Models A and B show a black hole formation efficiency of 27% and 37%, respectively. Model C has $\epsilon_{BH} = 35\%$. Model D shows the highest value of $\epsilon_{BH} = 46\%$. Models E and F have $\epsilon_{BH} = 19\%$ and $\epsilon_{BH} = 33\%$, respectively. Model G has a black hole formation efficiency of 8%. The black hole formation efficiency is 0% for model H, while the black hole formation efficiency is less than 1% for model I.

In Table 3.2.2 we summarize our results until 10 Myr, the columns are the same as for Table 3.2.1.

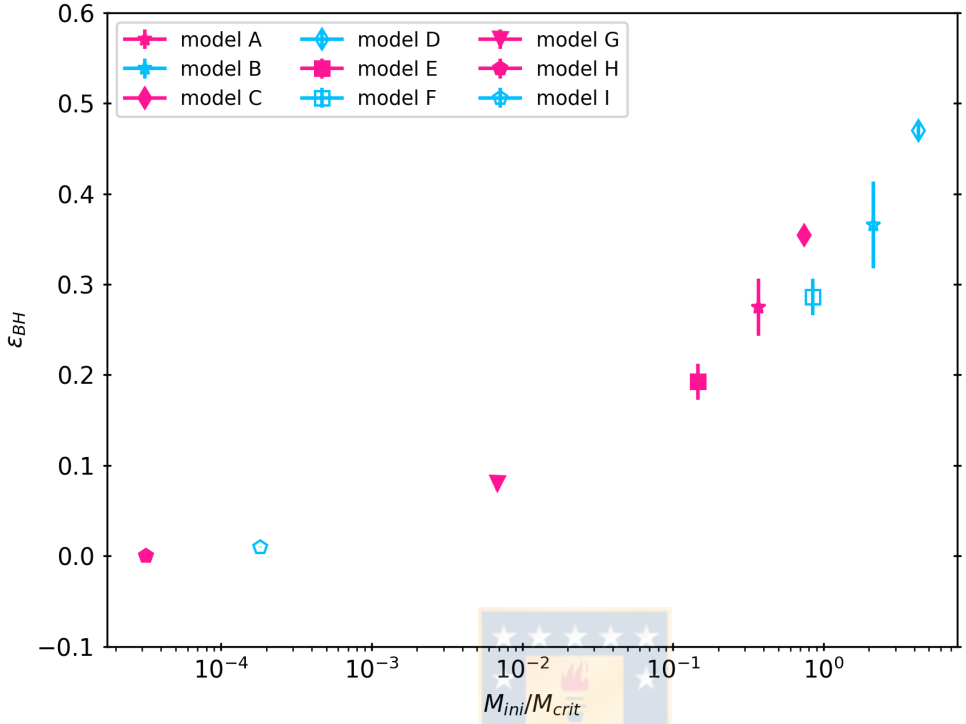

Figure 3.2.2: Black hole efficiency described by equation 1.5.1 against the initial mass of the nuclear star cluster normalized by the critical mass after 10 Myr.

Source: Vergara et. al. in prep.

Table 3.2.2: The columns are the same as Table 3.2.1. All quantities are measured until 10 Myr.

Models ID	M_{esc} [$M_\odot$]	M_{BH} [$M_\odot$]	M_{NSC} [$M_\odot$]	M_{CMO} [$M_\odot$]	ϵ_{BH}
A	2767 ± 111	610 ± 43	1623 ± 153	2233 ± 111	$27 \pm 0.3\%$
B	14300 ± 687	3850 ± 324	6850 ± 795	10700 ± 687	$36 \pm 0.4\%$
C	5340 ± 42	1650 ± 14	3010 ± 57	4660 ± 42	$35 \pm 0.1\%$
D	28050 ± 1600	10000 ± 100	11950 ± 1500	21950 ± 1600	46 ± 0.3
E	4213 ± 205	1110 ± 83	4677 ± 279	5787 ± 205	$19 \pm 0.2\%$
F	26167 ± 1547	7800 ± 788	16033 ± 2335	23833 ± 1547	$33 \pm 0.6\%$
G	8030 ± 48	6567 ± 94	85400 ± 90	91970 ± 48	$8 \pm 0.2\%$
H	26 ± 16	0	99973 ± 17	99973 ± 17	0%
I	383 ± 165	100	499617 ± 165	499517 ± 165	$0.99 \pm 0.0\%$

Models H and I show a very low black hole formation efficiency, close to $0 - 1\%$, since they are in a region where collisions are almost completely avoided ($t_H > t_{coll}$).

Model G shows a slightly higher, but still low black hole formation efficiency, reaching a value of only 8%, since its collision time scale (equation 1.4.1) is larger than its relaxation time scale (equation 1.4.3). Models A and E show the next highest ϵ_{BH} since they are very close to the region where collisions dominate stellar dynamics ($t_{coll} > t_H$). Models C and F are at the edge of the collision dominated region showing the next highest black hole formation efficiencies. Model B has the next highest $_{BH}$, followed by model D with the high black hole formation efficiency $\epsilon = 46\%$. These systems are in the region where collisions dominate the stellar dynamics of the system (see Fig. 2.7.1).

Chapter 4

Conclusions

In this thesis, we investigate the behavior of nuclear star clusters and their ability to form supermassive black holes under runaway collisions (Escala, 2021); we analyze the mass loss due to stars escaping from the system, the number of stellar collisions, the black hole formation efficiency, and the Lagrangian radii corresponding to 90%, 50% and 10% of the enclosed mass.

We perform an analysis of different models covering different regions described in Fig 1.4.1 in Section 1.4. These regions are delimited by the curves defined by equations 1.4.1 and 1.4.3, the collision time t_{coll} and relaxation time t_{relax}, respectively. If the collision time is shorter than the relaxation time, the stellar system becomes unstable under collisions, causing a chaotic collapse, ejecting several stars and forming a massive object. On the other hand, if $t_{relax} > t_{coll}$, the system practically avoids almost all of the collisions and experiences very few escapes. When the system is closer to the curve defined by equation 1.4.3, fewer collisions will occur, while if the model is closer to the curve from equation 1.4.1, more collisions will happen.

For the comparison with observations, we define the efficiency ϵ_{BH} as the ratio of black hole mass to stellar mass. The models with more chaotic evolution show that at the beginning the black hole formation efficiency is dominated by the stellar collisions, while at late times, the increase of the black hole formation efficiency is quickly dominated by the mass loss due to stellar escapes. Systems with longer relaxation time show a very low black hole formation efficiency that can even be equal to zero.

Some studies suggest that massive seeds ($\sim 10^5$ $M_\odot$) are needed to explain the observed supermassive black holes at high redshift (Shapiro, 2005; Pezzulli et al., 2016; Valiante et al., 2016; Sassano et al., 2021). Our chaotic models reach black hole masses of the order of 10^3 $M_\odot$, results consistent with the simulations of Portegies Zwart and McMillan (2002); Devecchi and Volonteri (2009); Sakurai et al. (2017); Reinoso et al. (2018). We expect that denser models in the parameter space dominated by collisions reach higher black hole mass ($> 10^5$ $M_\odot$) (Lee, 1987; Quinlan and Shapiro, 1990; Davies et al., 2011; Stone et al., 2017) and therefore a high black hole formation efficiency.

Our most extreme model is in the region where collisions dominate, while our most quiet model is in the region where collisions are avoided. The extreme model has an initial mass of 5×10^4 $M_\odot$, with a viral radius of 0.005 pc; this system forms a massive object of 9900 $M_\odot$ and loses a mass of 29650 $M_\odot$ due to the escapers. The black hole formation efficiency of this system is 46% and it is the highest of all our models. On the other hand, the quiet model has a mass of 1×10^5 $M_\odot$, with $R_v = 1$ pc, this system loses less than 1% of its initial mass due to stellar escapes, they shows no collisions, so the black hole formation efficiency is 0%. As expected, the black hole formation efficiency is quite high in the parameter space where collisions dominated. Here we explored setups where $t_{coll} = 1 - 10\,\mathrm{Myr}$ and $t_{relax} = 1 - 10\,\mathrm{Myr}$. The Universe has an age of 13.6 Gyr, which means that even more extended systems with larger collision and relaxation time scales can go through this collapse.

Chapter 5

Discussions

In this section, we discuss relevant future observations of supermassive black holes with the Extremely Large Telescope (ELT) which will be equipped with MICADO, the Multi-AO Imaging Camera for Deep Observations at near-infrared wavelengths. We also discuss future more realistic simulations with NBODY6++GPU.

5.1 Future observations

To prove the presence of supermassive black holes, their mass is usually measured using the velocity dispersion of the stellar motions (Ferrarese and Merritt, 2000; Tremaine et al., 2002; McConnell and Ma, 2013; Gültekin et al., 2009; Lützgendorf et al., 2013). The relation due to the mass of the central black hole and the velocity dispersion of the surrounding stars is a key question (Tremaine et al., 2002; Davies et al., 2018). Different measurements of the slope between black hole mass and velocity dispersion for elliptical galaxies, classical bulges of disk galaxies and, globular clusters are shown in Fig.5.1.1. The Tremaine et al. (2002) observations show a relation of $M_{BH} \propto \sigma^4$, while the McConnell and Ma (2013) observations show a relation of $M_{BH} \propto \sigma^{5.6}$ for galaxies. Reports of measurements of intermediate-mass black holes in globular clusters have been analyzed by Lützgendorf et al. (2013) indicating a possible relation of $M_{BH} \propto \sigma^{2.3}$. The slope of a globular cluster black hole mass and its velocity dispersion is shallower than the slope of a galaxy black hole mass and its velocity dispersion, which may suggest that there are different physical processes between globular clusters and galaxies. However, measurements of the mass of black holes in globular clusters

have an estimated significance of $< 3\sigma$; this is because it is difficult to measure the mass of the black hole in the populated center of globular clusters.

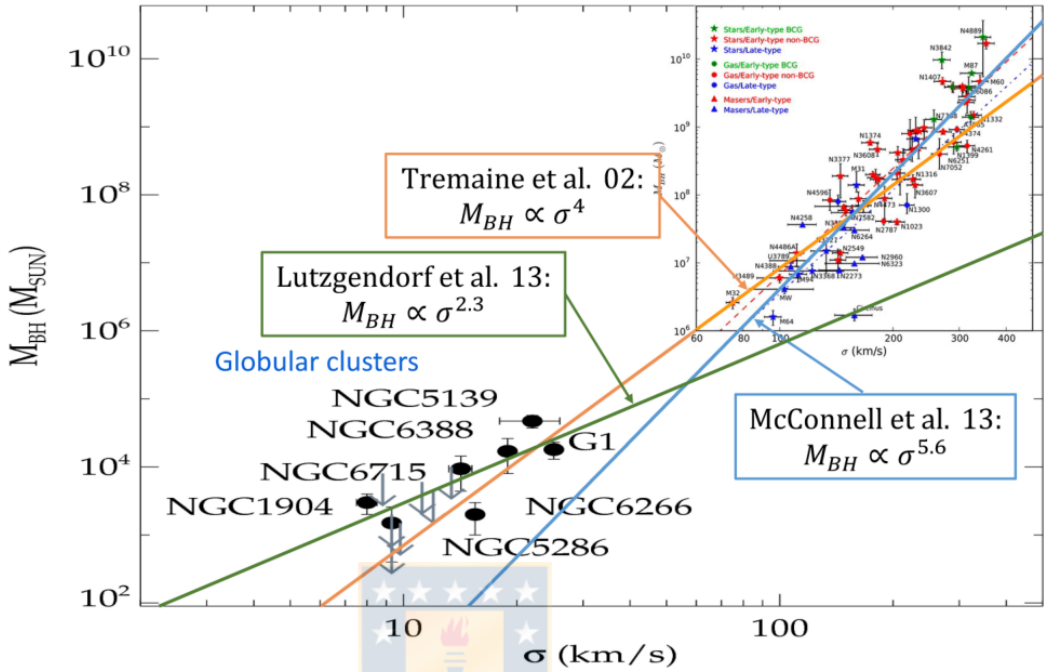

Figure 5.1.1: Correlation of the black hole mass M_{BH} with the central velocity dispersion σ, for galaxies (orange and blue lines) Tremaine et al. (2002) and, McConnell and Ma (2013), respectively, and for preliminary detections in globular clusters (green line) (Lützgendorf et al., 2013).

Source: Davies et al. (2018).

Fig. 5.1.2, shows that the measures with the ELT/MICADO will have enough spatial resolution to measure the black hole mass in crowded globular clusters.

The understanding of the coevolution of the host galaxies with their nuclear star clusters and the black hole at the center requires more detailed observations since it is very limited by the spatial resolution of the current instruments. The safer measures of mass use Keplerian orbits of stars around the supermassive black hole, such as the measure of the mass of Sagittarius A* in our own galaxy, the Milky Way (Ghez et al., 2008; Genzel et al., 2010; Gillessen et al., 2017). Another confident method is to measure the circular motions of water masers (Miyoshi et al., 1995; Greene et al., 2010; Kuo et al., 2011); however, this method is just useful for a few galaxies. There are secondary techniques, called dynamical measurements, which cover a large number of galaxies but with less spatial resolution, such as the reverberation mapping method (Blandford and McKee, 1982; Netzer and Peterson,

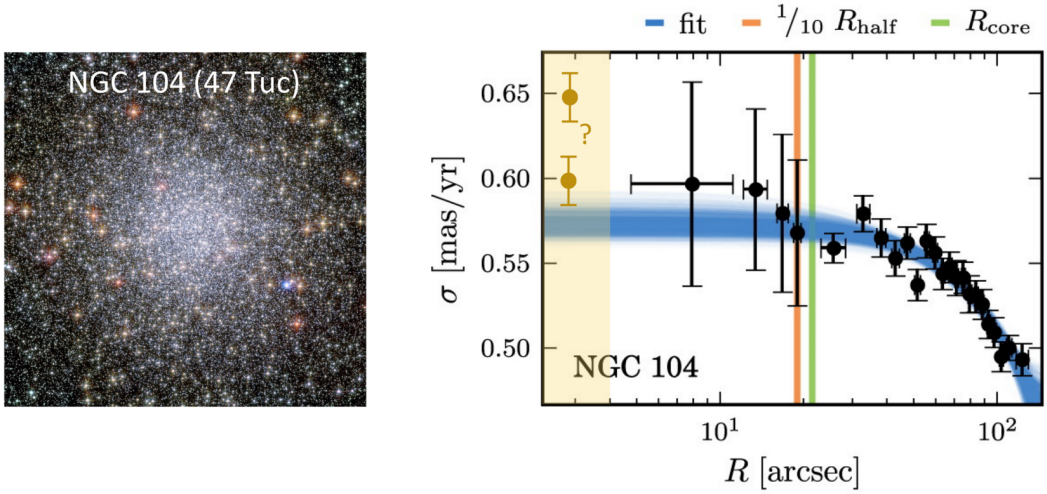

Figure 5.1.2: Left panel: Hubble Space Telescope (HST) image of NGC104 (47 Tuc). Right panel: state-of-the-art plot of the stellar velocity dispersion against the radial profile (Watkins et al., 2015). The blue band shows the range of polynomial fits. Black circles show a small error bar for the radial profile. The yellow region shows the extreme zone that MICADO can observe as the yellow circles (Tolstoy and Davies, 2019).

Source: Davies et al. (2018).

1997), or the measures of line widths of the broad line region in AGN (Reines and Volonteri, 2015). It is expected that the high resolution of ALMA could resolve this small region at the center of the galaxies (Barth et al., 2016), however gas kinematics is harder to solve and interpret than the stellar kinematics.

The sphere of influence where the black hole mass affects the motion of gas and stars through its gravity ranges from 1 pc to 1 kpc for M_{BH} of 10^6 $M_\odot$ to 10^{10} $M_\odot$, respectively. Fig. 5.1.3 shows that the current instrument VLT/SINFONI cannot resolve this range of influence, while ELT/MICADO can resolve it. Saglia et al. (2016) researched the correlation between the black hole mass, the velocity dispersion and the bulge mass of more than 90 galaxies, 25 of them from the SINFONI black hole surveys. This is one of the most rigorous compilations of data of these correlations. These correlations are useful for calibrating secondary techniques such as the width measurements of the broad line region in AGN (Reines and Volonteri, 2015). This technique is used to measure the mass of supermassive black holes at high redshift, covering a large cosmological volume. However, it has been suggested that the velocity dispersion measures are too high by around a factor of three, as it is difficult to resolve the sphere of influence

(Shankar et al., 2016). The high spatial resolution of MICADO will allow these spheres of influence to be resolved with greater precision, considerably increasing the available surveys of supermassive black holes masses (Tolstoy and Davies, 2019).

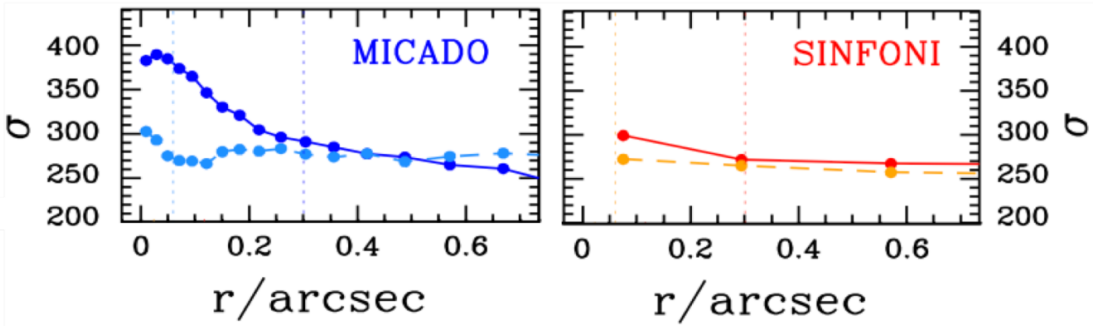

Figure 5.1.3: Both panels show the simulated velocity dispersion for the gravitational potential of NGC1600 modeled by Thomas et al. (2016). Left panel: the velocity dispersion profile that would be observed with ELT/MICADO. Right panel: the velocity dispersion profile that would be observed with VLT/SINFONI. The blue and red lines are for a black hole mass of $1.7 \times 10^9 M_\odot$ while the cyan and orange lines are for a black hole mass of $1.7 \times 10^7 M_\odot$. The vertical dashed lines represent the spheres of influence of the two black holes masses.

Source: Tolstoy and Davies (2019).

There are three main paths of supermassive black hole formation. The direct collapse of a gas cloud (Bromm and Loeb, 2003; Volonteri et al., 2008a; Latif et al., 2013; Latif and Schleicher, 2015), the supernovae remnants of Pop. III stars (Fryer et al., 2001; Heger and Woosley, 2002) and the runaway collision and mergers of stars in a cluster (Rees, 1984; Devecchi and Volonteri, 2009; Katz et al., 2015; Sakurai et al., 2017, 2019; Reinoso et al., 2018, 2020; Escala, 2021; Vergara et al., 2021). The different models of the formation of supermassive black holes point to different progenitor mass distributions (Volonteri et al., 2008b) (see the histograms of Fig. 5.1.4). The high spatial resolution of MICADO will allow to resolve the sphere of influence at a 5 times larger distance than the current instruments, also 2 times larger than the James Webb Space Telescope (JWST), which recently was sent into space. MICADO will measure the black hole mass of galaxies with velocities dispersions of > 270 km/s at redshift $z = 0.2$, which corresponds to a co-moving distance of 1 Gpc, covering a black hole mass range of 10^5-10^7 $M_\odot$ (Tolstoy and Davies, 2019) (see Fig. 5.1.4).

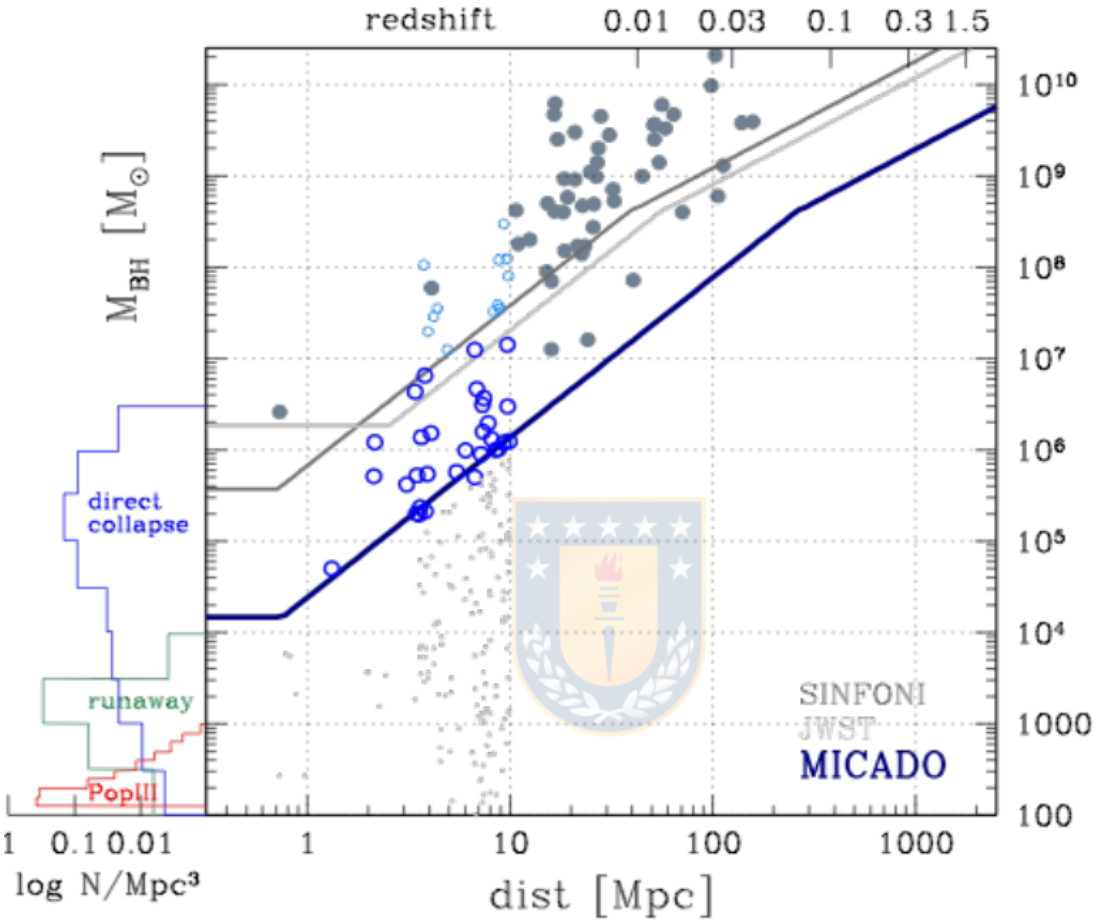

Figure 5.1.4: Measures of SMBHs masses using stellar dynamics as a function of co-moving distance and redshift.The grey filled circles show galaxies observed by OPINAS VLT/SINFONI. The dark and light blue void circles show galaxies that would be observable with MICADO and JWST. The grey dots are in the mass range that would not be observable with any telescope (even MICADO). The solid lines represent the limit resolution for the three instruments SINFONI, JWST, and MICADO (dark grey, light grey, and blue, respectively) as a function of redshift. The histograms at the left show the expected mass distribution of low mass black holes from different seed black hole populations.

Source: Tolstoy and Davies (2019).

5.2 Future simulations

Stellar populations are complex since they are born with an initial distribution of the masses of their stars that is called the initial mass function (IMF) (Salpeter, 1955). The IMF is similar within the Milky Way and nearby star-forming regions (Kroupa, 2001; Chabrier, 2003). The evolution of clusters depends strongly on their primordial binaries since a small fraction of binary systems can play a crucial role in the dynamics of the clusters (Goodman and Hut, 1989; Portegies Zwart et al., 2001). It is also important to consider stellar evolution, which is well known to strongly correlate with the initial mass of the star (Serenelli et al., 2021). As mentioned, NSCs live in the center of galaxies. It has been suggested that the formation of NSCs is due to the accretion of globular clusters, which fall to the center by dynamic friction (Antonini et al., 2012). This mechanism is called a cluster-inspiral and is generally attributed as an explanation for the rotation observed in NSCs (Seth et al., 2008). Therefore, including rotation in NSC simulations will be important when developing more realistic simulations, since the presence of rotation in the spherical models leads to a deformation in the outer zone of the cluster, appearing in a non-spherical distribution (Varri and Bertin, 2012; Lupton and Gunn, 1987). Rotation and stellar collisions have not been investigated much yet, however, I have already explored collisions in rotating models (Vergara et al., 2021)

The research of collisions in NSCs as a pathway for SMBH formation in general is an important field of study that must be investigated more deeply in a realistic way. To develop this work during my PhD I will pursue simulations with an initial mass function (IMF), including rotation, primordial binaries, stellar evolution and rotation. In the context of stellar evolution, the mass loss due to stellar winds can be particularly interesting. If a star in a binary system is losing mass, the other star can accrete this material. If the stars are close enough, the Roche-lobe will be filled allowing for mass transfer. However, if the star cannot accrete all the material, it remains in a common envelope surrounding the stars (Rizzuto et al., 2021). The mass loss by the most massive object can drastically reduce the final mass (Glebbeek et al., 2009), so it is an important factor to take into account. We also plan to include other prescriptions such as the fast and delayed core-collapse for treating the supernova, as in the work of Kamlah et al. (2021). I

will follow realistic simulations of stars clusters (Wang et al., 2016; Rizzuto et al., 2021; Kamlah et al., 2021), which use a distribution of stars following the density profile of King (1966). I will also include the IMF developed by Kroupa (2001), using zero-age main-sequence stars with masses between $0.08 - 150 M_{\odot}$, besides including a primordial binary fraction of $5 - 10\%$ of the total number of stars. For the stellar evolution, it is important to consider mass loss produced by stellar winds, following the models of Eggleton et al. (1990); Hurley et al. (2000, 2002).

MICADO, ELT, and JWST will observe many additional NSCs and determine many supermassive black hole masses that will allow the efficiency of black hole formation to be determined with high precision. The large observational data set could be compared with the results of our model. Our model suggests that NSCs could form a more massive object than 10^4 $M_{\odot}$ through runaway collisions (see Fig. 5.1.4). These observations will also help to probe the new formation scenario proposed here, by providing an accurate estimation of black hole masses for a large range of different clusters.

Bibliography

Aarseth, S. J. (1963). Dynamical evolution of clusters of galaxies, I. , 126:223.

Aarseth, S. J. (1985). Direct N-body calculations. In Goodman, J. and Hut, P., editors, *Dynamics of Star Clusters*, volume 113, pages 251–258.

Aarseth, S. J. (2000). NBODY 6: A New Star Cluster Simulation Code. In Gurzadyan, V. G. and Ruffini, R., editors, *The Chaotic Universe*, pages 286–287.

Ahmad, A. and Cohen, L. (1973). A numerical integration scheme for the N-body gravitational problem. *Journal of Computational Physics*, 12:389–402.

Alister Seguel, P. J., Schleicher, D. R. G., Boekholt, T. C. N., Fellhauer, M., and Klessen, R. S. (2020). Formation of SMBH seeds in Population III star clusters through collisions: the importance of mass loss. , 493(2):2352–2362.

Antonini, F., Barausse, E., and Silk, J. (2015). The Coevolution of Nuclear Star Clusters, Massive Black Holes, and Their Host Galaxies. , 812(1):72.

Antonini, F., Capuzzo-Dolcetta, R., Mastrobuono-Battisti, A., and Merritt, D. (2012). Dissipationless Formation and Evolution of the Milky Way Nuclear Star Cluster. , 750(2):111.

Antonini, F., Gieles, M., and Gualandris, A. (2019). Black hole growth through hierarchical black hole mergers in dense star clusters: implications for gravitational wave detections. , 486(4):5008–5021.

Bañados, E., Venemans, B. P., Decarli, R., Farina, E. P., Mazzucchelli, C., Walter, F., Fan, X., Stern, D., Schlafly, E., Chambers, K. C., Rix, H. W., Jiang, L., McGreer, I., Simcoe, R., Wang, F., Yang, J., Morganson, E., De Rosa, G., Greiner, J., Baloković, M., Burgett, W. S., Cooper, T., Draper, P. W., Flewelling, H., Hodapp, K. W., Jun, H. D., Kaiser, N., Kudritzki, R. P., Magnier, E. A., Metcalfe, N., Miller, D., Schindler, J. T., Tonry, J. L., Wainscoat, R. J., Waters, C., and Yang, Q. (2016). The Pan-STARRS1 Distant z $>$ 5.6 Quasar Survey: More than 100 Quasars within the First Gyr of the Universe. , 227(1):11.

Bañados, E., Venemans, B. P., Mazzucchelli, C., Farina, E. P., Walter, F., Wang, F., Decarli, R., Stern, D., Fan, X., Davies, F. B., Hennawi, J. F., Simcoe, R. A., Turner, M. L., Rix, H.-W., Yang, J., Kelson, D. D., Rudie, G. C., and Winters,

J. M. (2018). An 800-million-solar-mass black hole in a significantly neutral Universe at a redshift of 7.5. , 553(7689):473–476.

Banerjee, S. and Kroupa, P. (2017). How can young massive clusters reach their present-day sizes? , 597:A28.

Barth, A. J., Boizelle, B. D., Darling, J., Baker, A. J., Buote, D. A., Ho, L. C., and Walsh, J. L. (2016). Measurement of the Black Hole Mass in NGC 1332 from ALMA Observations at 0.044 arcsecond Resolution. , 822(2):L28.

Barth, A. J., Strigari, L. E., Bentz, M. C., Greene, J. E., and Ho, L. C. (2009). Dynamical Constraints on the Masses of the Nuclear Star Cluster and Black Hole in the Late-Type Spiral Galaxy NGC 3621. , 690(1):1031–1044.

Baumgardt, H., Amaro-Seoane, P., and Schödel, R. (2018). The distribution of stars around the Milky Way's central black hole. III. Comparison with simulations. , 609:A28.

Begelman, M. C. (2010). Evolution of supermassive stars as a pathway to black hole formation. , 402(1):673–681.

Begelman, M. C., Volonteri, M., and Rees, M. J. (2006). Formation of supermassive black holes by direct collapse in pre-galactic haloes. , 370(1):289–298.

Bender, R., Kormendy, J., Bower, G., Green, R., Thomas, J., Danks, A. C., Gull, T., Hutchings, J. B., Joseph, C. L., Kaiser, M. E., Lauer, T. R., Nelson, C. H., Richstone, D., Weistrop, D., and Woodgate, B. (2005). HST STIS Spectroscopy of the Triple Nucleus of M31: Two Nested Disks in Keplerian Rotation around a Supermassive Black Hole. , 631(1):280–300.

Binney, J. and Tremaine, S. (2008). *Galactic Dynamics: Second Edition.*

Blandford, R. D. and McKee, C. F. (1982). Reverberation mapping of the emission line regions of Seyfert galaxies and quasars. , 255:419–439.

Boekholt, T. C. N., Schleicher, D. R. G., Fellhauer, M., Klessen, R. S., Reinoso, B., Stutz, A. M., and Haemmerlé, L. (2018). Formation of massive seed black holes via collisions and accretion. , 476(1):366–380.

Böker, T., Laine, S., van der Marel, R. P., Sarzi, M., Rix, H.-W., Ho, L. C., and Shields, J. C. (2002). A Hubble Space Telescope Census of Nuclear Star Clusters in Late-Type Spiral Galaxies. I. Observations and Image Analysis. , 123(3):1389–1410.

Bond, J. R., Arnett, W. D., and Carr, B. J. (1984). The evolution and fate of Very Massive Objects. , 280:825–847.

Bovino, S., Grassi, T., Schleicher, D. R. G., and Banerjee, R. (2016). The Formation of the Primitive Star SDSS J102915+172927: Effect of the Dust Mass and the Grain-size Distribution. , 832(2):154.

Bovino, S., Grassi, T., Schleicher, D. R. G., and Latif, M. A. (2014). Formation of Carbon-enhanced Metal-poor Stars in the Presence of Far-ultraviolet Radiation. , 790(2):L35.

Bromm, V., Coppi, P. S., and Larson, R. B. (2002). The Formation of the First Stars. I. The Primordial Star-forming Cloud. , 564(1):23–51.

Bromm, V. and Loeb, A. (2003). Formation of the First Supermassive Black Holes. , 596(1):34–46.

Chabrier, G. (2003). Galactic Stellar and Substellar Initial Mass Function. , 115(809):763–795.

Chon, S. and Omukai, K. (2020). Supermassive star formation via super competitive accretion in slightly metal-enriched clouds. , 494(2):2851–2860.

Clark, P. C., Glover, S. C. O., and Klessen, R. S. (2008). The First Stellar Cluster. , 672(2):757–764.

Clark, P. C., Glover, S. C. O., Klessen, R. S., and Bromm, V. (2011). Gravitational Fragmentation in Turbulent Primordial Gas and the Initial Mass Function of Population III Stars. , 727(2):110.

Cohn, H. (1979). Numerical integration of the Fokker-Planck equation and the evolution of star clusters. , 234:1036–1053.

Côté, P., Piatek, S., Ferrarese, L., Jordán, A., Merritt, D., Peng, E. W., Haşegan, M., Blakeslee, J. P., Mei, S., West, M. J., Milosavljević, M., and Tonry, J. L. (2006). The ACS Virgo Cluster Survey. VIII. The Nuclei of Early-Type Galaxies. , 165(1):57–94.

Das, A., Schleicher, D. R. G., Leigh, N. W. C., and Boekholt, T. C. N. (2021). Formation of supermassive black hole seeds in nuclear star clusters via gas accretion and runaway collisions. , 503(1):1051–1069.

Davies, M. B., Miller, M. C., and Bellovary, J. M. (2011). Supermassive Black Hole Formation Via Gas Accretion in Nuclear Stellar Clusters. , 740(2):L42.

Davies, R., Alves, J., Clénet, Y., Lang-Bardl, F., Nicklas, H., Pott, J. U., Ragazzoni, R., Tolstoy, E., Amico, P., Anwand-Heerwart, H., Barboza, S., Barl, L., Baudoz, P., Bender, R., Bezawada, N., Bizenberger, P., Boland, W., Bonifacio, P., Borgo, B., Buey, T., Chapron, F., Chemla, F., Cohen, M., Czoske, O., Déo, V., Disseau, K., Dreizler, S., Dupuis, O., Fabricius, M., Falomo, R., Fedou, P., Förster Schreiber, N., Garrel, V., Geis, N., Gemperlein, H., Gendron, E., Genzel, R., Gillessen, S., Glück, M., Grupp, F., Hartl, M., Häuser, M., Hess, H. J., Hofferbert, R., Hopp, U., Hörmann, V., Hubert, Z., Huby, E., Huet, J. M., Hutterer, V., Ives, D., Janssen, A., Jellema, W., Kausch, W., Kerber, F., Kravcar, H., Le Ruyet, B., Leschinski, K., Mandla, C., Manhart, M., Massari, D., Mei, S., Merlin, F., Mohr, L., Monna, A., Muench, N., Müller, F., Musters, G., Navarro, R., Neumann, U., Neumayer, N., Niebsch, J., Plattner, M., Przybilla, N., Rabien, S., Ramlau, R., Ramos, J., Ramsay, S.,

Rhode, P., Richter, A., Richter, J., Rix, H. W., Rodeghiero, G., Rohloff, R. R., Rosensteiner, M., Rousset, G., Schlichter, J., Schubert, J., Sevin, A., Stuik, R., Sturm, E., Thomas, J., Tromp, N., Verdoes-Kleijn, G., Vidal, F., Wagner, R., Wegner, M., Zeilinger, W., Ziegleder, J., Ziegler, B., and Zins, G. (2018). The MICADO first light imager for the ELT: overview, operation, simulation. In Evans, C. J., Simard, L., and Takami, H., editors, *Ground-based and Airborne Instrumentation for Astronomy VII*, volume 10702 of *Society of Photo-Optical Instrumentation Engineers (SPIE) Conference Series*, page 107021S.

Demircan, O. and Kahraman, G. (1991). Stellar Mass / Luminosity and Mass / Radius Relations. , 181(2):313–322.

Devecchi, B. and Volonteri, M. (2009). Formation of the First Nuclear Clusters and Massive Black Holes at High Redshift. , 694(1):302–313.

Eggleton, P. P., Fitchett, M. J., and Tout, C. A. (1990). The Distribution of Visual Binaries with Two Bright Components: Erratum. , 354:387.

Escala, A. (2021). Observational Support for Massive Black Hole Formation Driven by Runaway Stellar Collisions in Galactic Nuclei. , 908(1):57.

Event Horizon Telescope Collaboration, Akiyama, K., Alberdi, A., Alef, W., Asada, K., Azulay, R., Baczko, A.-K., Ball, D., Baloković, M., Barrett, J., and et al. (2019). First M87 Event Horizon Telescope Results. I. The Shadow of the Supermassive Black Hole. , 875(1):L1.

Fan, X., Strauss, M. A., Schneider, D. P., Becker, R. H., White, R. L., Haiman, Z., Gregg, M., Pentericci, L., Grebel, E. K., Narayanan, V. K., Loh, Y.-S., Richards, G. T., Gunn, J. E., Lupton, R. H., Knapp, G. R., Ivezić, Ž., Brandt, W. N., Collinge, M., Hao, L., Harbeck, D., Prada, F., Schaye, J., Strateva, I., Zakamska, N., Anderson, S., Brinkmann, J., Bahcall, N. A., Lamb, D. Q., Okamura, S., Szalay, A., and York, D. G. (2003). A Survey of z>5.7 Quasars in the Sloan Digital Sky Survey. II. Discovery of Three Additional Quasars at z>6. , 125(4):1649–1659.

Ferrarese, L., Côté, P., Dalla Bontà, E., Peng, E. W., Merritt, D., Jordán, A., Blakeslee, J. P., Haşegan, M., Mei, S., Piatek, S., Tonry, J. L., and West, M. J. (2006). A Fundamental Relation between Compact Stellar Nuclei, Supermassive Black Holes, and Their Host Galaxies. , 644(1):L21–L24.

Ferrarese, L. and Merritt, D. (2000). A Fundamental Relation between Supermassive Black Holes and Their Host Galaxies. , 539(1):L9–L12.

Filippenko, A. V. and Ho, L. C. (2003). A Low-Mass Central Black Hole in the Bulgeless Seyfert 1 Galaxy NGC 4395. , 588(1):L13–L16.

Fryer, C. L., Woosley, S. E., and Heger, A. (2001). Pair-Instability Supernovae, Gravity Waves, and Gamma-Ray Transients. , 550(1):372–382.

Gao, L., Yoshida, N., Abel, T., Frenk, C. S., Jenkins, A., and Springel, V. (2007). The first generation of stars in the Λ cold dark matter cosmology. , 378(2):449–468.

Genzel, R., Eisenhauer, F., and Gillessen, S. (2010). The Galactic Center massive black hole and nuclear star cluster. *Reviews of Modern Physics*, 82(4):3121–3195.

Georgiev, I. Y., Böker, T., Leigh, N., Lützgendorf, N., and Neumayer, N. (2016). Masses and scaling relations for nuclear star clusters, and their co-existence with central black holes. , 457(2):2122–2138.

Ghez, A. M., Salim, S., Weinberg, N. N., Lu, J. R., Do, T., Dunn, J. K., Matthews, K., Morris, M. R., Yelda, S., Becklin, E. E., Kremenek, T., Milosavljevic, M., and Naiman, J. (2008). Measuring Distance and Properties of the Milky Way's Central Supermassive Black Hole with Stellar Orbits. , 689(2):1044–1062.

Gillessen, S., Plewa, P. M., Eisenhauer, F., Sari, R., Waisberg, I., Habibi, M., Pfuhl, O., George, E., Dexter, J., von Fellenberg, S., Ott, T., and Genzel, R. (2017). An Update on Monitoring Stellar Orbits in the Galactic Center. , 837(1):30.

Glebbeek, E., Gaburov, E., de Mink, S. E., Pols, O. R., and Portegies Zwart, S. F. (2009). The evolution of runaway stellar collision products. , 497(1):255–264.

Goodman, J. and Hut, P. (1989). Primordial binaries and globular cluster evolution. , 339(6219):40–42.

Graham, A. W. and Spitler, L. R. (2009). Quantifying the coexistence of massive black holes and dense nuclear star clusters. , 397(4):2148–2162.

Grassi, T., Bovino, S., Haugbølle, T., and Schleicher, D. R. G. (2017). A detailed framework to incorporate dust in hydrodynamical simulations. , 466(2):1259–1274.

Greene, J. E., Peng, C. Y., Kim, M., Kuo, C.-Y., Braatz, J. A., Impellizzeri, C. M. V., Condon, J. J., Lo, K. Y., Henkel, C., and Reid, M. J. (2010). Precise Black Hole Masses from Megamaser Disks: Black Hole-Bulge Relations at Low Mass. , 721(1):26–45.

Greif, T. H., Bromm, V., Clark, P. C., Glover, S. C. O., Smith, R. J., Klessen, R. S., Yoshida, N., and Springel, V. (2012). Formation and evolution of primordial protostellar systems. , 424(1):399–415.

Grete, P., Latif, M. A., Schleicher, D. R. G., and Schmidt, W. (2019). Intermittent fragmentation and statistical variations during gas collapse in magnetized atomic cooling haloes. , 487(4):4525–4535.

Gültekin, K., Richstone, D. O., Gebhardt, K., Lauer, T. R., Tremaine, S., Aller, M. C., Bender, R., Dressler, A., Faber, S. M., Filippenko, A. V., Green, R., Ho, L. C., Kormendy, J., Magorrian, J., Pinkney, J., and Siopis, C. (2009).

The M-σ and M-L Relations in Galactic Bulges, and Determinations of Their Intrinsic Scatter. , 698(1):198–221.

Häring, N. and Rix, H.-W. (2004). On the Black Hole Mass-Bulge Mass Relation. , 604(2):L89–L92.

Heger, A. and Woosley, S. E. (2002). The Nucleosynthetic Signature of Population III. , 567(1):532–543.

Hirano, S., Hosokawa, T., Yoshida, N., Umeda, H., Omukai, K., Chiaki, G., and Yorke, H. W. (2014). One Hundred First Stars: Protostellar Evolution and the Final Masses. , 781(2):60.

Hurley, J. R., Pols, O. R., and Tout, C. A. (2000). Comprehensive analytic formulae for stellar evolution as a function of mass and metallicity. , 315(3):543–569.

Hurley, J. R., Tout, C. A., and Pols, O. R. (2002). Evolution of binary stars and the effect of tides on binary populations. , 329(4):897–928.

Kamlah, A. W. H., Leveque, A., Spurzem, R., Arca Sedda, M., Askar, A., Banerjee, S., Berczik, P., Giersz, M., Hurley, J., Belloni, D., Kühmichel, L., and Wang, L. (2021). Preparing the next gravitational million-body simulations: Evolution of single and binary stars in Nbody6++GPU, MOCCA and McLuster. .

Katz, H., Sijacki, D., and Haehnelt, M. G. (2015). Seeding high-redshift QSOs by collisional runaway in primordial star clusters. , 451(3):2352–2369.

Khalisi, E., Wang, L., and Spurzem, R. (2019). *NBODY6++ Manual for the Computer Code ,Version 4.1, latest update: October 11, 2019.*

King, A. (2016). How big can a black hole grow? , 456(1):L109–L112.

King, I. R. (1966). The structure of star clusters. III. Some simple dynamical models. , 71:64.

Kormendy, J. and Ho, L. C. (2013). Coevolution (Or Not) of Supermassive Black Holes and Host Galaxies. , 51(1):511–653.

Koushiappas, S. M., Bullock, J. S., and Dekel, A. (2004). Massive black hole seeds from low angular momentum material. , 354(1):292–304.

Kroupa, P. (2001). On the variation of the initial mass function. , 322(2):231–246.

Kroupa, P., Subr, L., Jerabkova, T., and Wang, L. (2020). Very high redshift quasars and the rapid emergence of supermassive black holes. , 498(4):5652–5683.

Kuo, C. Y., Braatz, J. A., Condon, J. J., Impellizzeri, C. M. V., Lo, K. Y., Zaw, I., Schenker, M., Henkel, C., Reid, M. J., and Greene, J. E. (2011). The Megamaser Cosmology Project. III. Accurate Masses of Seven Supermassive Black Holes in Active Galaxies with Circumnuclear Megamaser Disks. , 727(1):20.

Kustaanheimo, P. and Stiefel, E. (1965). *J. Reine Angew. Math., 218, 204.*

Landau, L. D. and Lifshitz, E. M. (1980). *Statistical physics. Pt.1, Pt.2.*

Latif, M. A., Bovino, S., Van Borm, C., Grassi, T., Schleicher, D. R. G., and Spaans, M. (2014). A UV flux constraint on the formation of direct collapse black holes. , 443(3):1979–1987.

Latif, M. A., Khochfar, S., Schleicher, D., and Whalen, D. J. (2021). Radiation hydrodynamical simulations of the birth of intermediate-mass black holes in the first galaxies. , 508(2):1756–1767.

Latif, M. A., Omukai, K., Habouzit, M., Schleicher, D. R. G., and Volonteri, M. (2016). Impact of Dust Cooling on Direct-collapse Black Hole Formation. , 823(1):40.

Latif, M. A. and Schleicher, D. R. G. (2015). The formation of supermassive black holes in rapidly rotating disks. , 578:A118.

Latif, M. A., Schleicher, D. R. G., Schmidt, W., and Niemeyer, J. C. (2013). The characteristic black hole mass resulting from direct collapse in the early Universe. , 436(4):2989–2996.

Lee, H. M. (1987). Dynamical Effects of Successive Mergers on the Evolution of Spherical Stellar Systems. , 319:801.

Leigh, N., Böker, T., and Knigge, C. (2012). Nuclear star clusters and the stellar spheroids of their host galaxies. , 424(3):2130–2138.

Li, J., Wang, R., Cox, P., Gao, Y., Walter, F., Wagg, J., Menten, K. M., Bertoldi, F., Shao, Y., Venemans, B. P., Decarli, R., Riechers, D., Neri, R., Fan, X., Omont, A., and Narayanan, D. (2020). Ionized and Atomic Interstellar Medium in the z = 6.003 Quasar SDSS J2310+1855. , 900(2):131.

Li, Y., Haiman, Z., and Mac Low, M.-M. (2007). Correlations between Central Massive Objects and Their Host Galaxies: From Bulgeless Spirals to Ellipticals. , 663(1):61–70.

Lupi, A., Colpi, M., Devecchi, B., Galanti, G., and Volonteri, M. (2014). Constraining the high-redshift formation of black hole seeds in nuclear star clusters with gas inflows. , 442(4):3616–3626.

Lupton, R. H. and Gunn, J. E. (1987). Three-Integral Models of Globular Clusters. , 93:1106.

Lützgendorf, N., Kissler-Patig, M., Neumayer, N., Baumgardt, H., Noyola, E., de Zeeuw, P. T., Gebhardt, K., Jalali, B., and Feldmeier, A. (2013). M - σrelation for intermediate-mass black holes in globular clusters. , 555:A26.

Lynden-Bell, D. and Wood, R. (1968). The gravo-thermal catastrophe in isothermal spheres and the onset of red-giant structure for stellar systems. , 138:495.

Madau, P. and Rees, M. J. (2001). Massive Black Holes as Population III Remnants. , 551(1):L27–L30.

Magorrian, J., Tremaine, S., Richstone, D., Bender, R., Bower, G., Dressler, A., Faber, S. M., Gebhardt, K., Green, R., Grillmair, C., Kormendy, J., and Lauer, T. (1998). The Demography of Massive Dark Objects in Galaxy Centers. , 115(6):2285–2305.

Makino, J. (1991). Optimal Order and Time-Step Criterion for Aarseth-Type N-Body Integrators. , 369:200.

Marconi, A. and Hunt, L. K. (2003). The Relation between Black Hole Mass, Bulge Mass, and Near-Infrared Luminosity. , 589(1):L21–L24.

McConnell, N. J. and Ma, C.-P. (2013). Revisiting the Scaling Relations of Black Hole Masses and Host Galaxy Properties. , 764(2):184.

Mikkola, S. and Aarseth, S. J. (1990). A chain regularization method for the few-body problem. *Celestial Mechanics and Dynamical Astronomy*, 47(4):375–390.

Mikkola, S. and Aarseth, S. J. (1993). An Implementation of N-Body Chain Regularization. *Celestial Mechanics and Dynamical Astronomy*, 57(3):439–459.

Miyoshi, M., Moran, J., Herrnstein, J., Greenhill, L., Nakai, N., Diamond, P., and Inoue, M. (1995). Evidence for a black hole from high rotation velocities in a sub-parsec region of NGC4258. , 373(6510):127–129.

Mortlock, D. J., Warren, S. J., Venemans, B. P., Patel, M., Hewett, P. C., McMahon, R. G., Simpson, C., Theuns, T., Gonzáles-Solares, E. A., Adamson, A., Dye, S., Hambly, N. C., Hirst, P., Irwin, M. J., Kuiper, E., Lawrence, A., and Röttgering, H. J. A. (2011). A luminous quasar at a redshift of z = 7.085. , 474(7353):616–619.

Natarajan, P. and Treister, E. (2009). Is there an upper limit to black hole masses? , 393(3):838–845.

Netzer, H. and Peterson, B. M. (1997). Reverberation Mapping and the Physics of Active Galactic Nuclei. In Maoz, D., Sternberg, A., and Leibowitz, E. M., editors, *Astronomical Time Series*, volume 218 of *Astrophysics and Space Science Library*, page 85.

Neumayer, N., Seth, A., and Böker, T. (2020). Nuclear star clusters. , 28(1):4.

Nguyen, D. D., Seth, A. C., den Brok, M., Neumayer, N., Cappellari, M., Barth, A. J., Caldwell, N., Williams, B. F., and Binder, B. (2017). Improved Dynamical Constraints on the Mass of the Central Black Hole in NGC 404. , 836(2):237.

Nitadori, K. and Aarseth, S. J. (2012). Accelerating NBODY6 with graphics processing units. , 424(1):545–552.

O'Leary, R. M., Meiron, Y., and Kocsis, B. (2016). Dynamical Formation Signatures of Black Hole Binaries in the First Detected Mergers by LIGO. , 824(1):L12.

Omukai, K. (2000). Protostellar Collapse with Various Metallicities. , 534(2):809–824.

Omukai, K. and Nishi, R. (1998). Formation of Primordial Protostars. , 508(1):141–150.

Omukai, K., Schneider, R., and Haiman, Z. (2008). Can Supermassive Black Holes Form in Metal-enriched High-Redshift Protogalaxies? , 686(2):801–814.

Onoue, M., Kashikawa, N., Matsuoka, Y., Kato, N., Izumi, T., Nagao, T., Strauss, M. A., Harikane, Y., Imanishi, M., Ito, K., Iwasawa, K., Kawaguchi, T., Lee, C.-H., Noboriguchi, A., Suh, H., Tanaka, M., and Toba, Y. (2019). Subaru High-z Exploration of Low-luminosity Quasars (SHELLQs). VI. Black Hole Mass Measurements of Six Quasars at $6.1 \leq z \leq 6.7$. , 880(2):77.

Pacucci, F., Natarajan, P., and Ferrara, A. (2017). Feedback Limits to Maximum Seed Masses of Black Holes. , 835(2):L36.

Panamarev, T., Just, A., Spurzem, R., Berczik, P., Wang, L., and Arca Sedda, M. (2019). Direct N-body simulation of the Galactic centre. , 484(3):3279–3290.

Parsons, J., Mas-Ribas, L., Sun, G., Chang, T.-C., Gonzalez, M. O., and Mebane, R. H. (2021). Probing Population III IMFs with He II/Hα Intensity Mapping. *arXiv e-prints*, page arXiv:2112.06407.

Pensabene, A., Decarli, R., Bañados, E., Venemans, B., Walter, F., Bertoldi, F., Fan, X., Farina, E. P., Li, J., Mazzucchelli, C., Novak, M., Riechers, D., Rix, H. W., Strauss, M. A., Wang, R., Weiß, A., Yang, J., and Yang, Y. (2021). An ALMA multi-line survey of the ISM in two quasar host-companion galaxy pairs at $z > 6$. *arXiv e-prints*, page arXiv:2105.09958.

Peters, T., Schleicher, D. R. G., Smith, R. J., Schmidt, W., and Klessen, R. S. (2014). Low-metallicity star formation: relative impact of metals and magnetic fields. , 442(4):3112–3126.

Pezzulli, E., Valiante, R., and Schneider, R. (2016). Super-Eddington growth of the first black holes. , 458(3):3047–3059.

Plummer, H. C. (1911). On the problem of distribution in globular star clusters. , 71:460–470.

Portegies Zwart, S. F., Makino, J., McMillan, S. L. W., and Hut, P. (1999). Star cluster ecology. III. Runaway collisions in young compact star clusters. , 348:117–126.

Portegies Zwart, S. F. and McMillan, S. L. W. (2002). The Runaway Growth of Intermediate-Mass Black Holes in Dense Star Clusters. , 576(2):899–907.

Portegies Zwart, S. F., McMillan, S. L. W., Hut, P., and Makino, J. (2001). Simulating Open Star Clusters. In Vanbeveren, D., editor, *The Influence of Binaries on Stellar Population Studies*, volume 264 of *Astrophysics and Space Science Library*, page 371.

Quinlan, G. D. and Shapiro, S. L. (1990). The Dynamical Evolution of Dense Star Clusters in Galactic Nuclei. , 356:483.

Rees, M. J. (1984). Black Hole Models for Active Galactic Nuclei. , 22:471–506.

Regan, J. A., Visbal, E., Wise, J. H., Haiman, Z., Johansson, P. H., and Bryan, G. L. (2017). Rapid formation of massive black holes in close proximity to embryonic protogalaxies. *Nature Astronomy*, 1:0075.

Reines, A. E. and Volonteri, M. (2015). Relations between Central Black Hole Mass and Total Galaxy Stellar Mass in the Local Universe. , 813(2):82.

Reinoso, B., Schleicher, D. R. G., Fellhauer, M., Klessen, R. S., and Boekholt, T. C. N. (2018). Collisions in primordial star clusters. Formation pathway for intermediate mass black holes. , 614:A14.

Reinoso, B., Schleicher, D. R. G., Fellhauer, M., Leigh, N. W. C., and Klessen, R. S. (2020). The effects of a background potential in star cluster evolution. A delay in the relaxation time-scale and runaway collision processes. , 639:A92.

Rizzuto, F. P., Naab, T., Spurzem, R., Giersz, M., Ostriker, J. P., Stone, N. C., Wang, L., Berczik, P., and Rampp, M. (2021). Intermediate mass black hole formation in compact young massive star clusters. , 501(4):5257–5273.

Saglia, R. P., Opitsch, M., Erwin, P., Thomas, J., Beifiori, A., Fabricius, M., Mazzalay, X., Nowak, N., Rusli, S. P., and Bender, R. (2016). The SINFONI Black Hole Survey: The Black Hole Fundamental Plane Revisited and the Paths of (Co)evolution of Supermassive Black Holes and Bulges. , 818(1):47.

Sakurai, Y., Haiman, Z., and Inayoshi, K. (2020). Radiative feedback for supermassive star formation in a massive cloud with H_2 molecules in an atomic-cooling halo. , 499(4):5960–5971.

Sakurai, Y., Hosokawa, T., Yoshida, N., and Yorke, H. W. (2015). Formation of primordial supermassive stars by burst accretion. , 452(1):755–764.

Sakurai, Y., Yoshida, N., and Fujii, M. S. (2019). Growth of intermediate mass black holes by tidal disruption events in the first star clusters. , 484(4):4665–4677.

Sakurai, Y., Yoshida, N., Fujii, M. S., and Hirano, S. (2017). Formation of intermediate-mass black holes through runaway collisions in the first star clusters. , 472(2):1677–1684.

Salpeter, E. E. (1955). The Luminosity Function and Stellar Evolution. , 121:161.

Sassano, F., Schneider, R., Valiante, R., Inayoshi, K., Chon, S., Omukai, K., Mayer, L., and Capelo, P. R. (2021). Light, medium-weight, or heavy? The nature of the first supermassive black hole seeds. , 506(1):613–632.

Schleicher, D. R. G., Palla, F., Ferrara, A., Galli, D., and Latif, M. (2013). Massive black hole factories: Supermassive and quasi-star formation in primordial halos. , 558:A59.

Schleicher, D. R. G., Spaans, M., and Glover, S. C. O. (2010a). Black Hole Formation in Primordial Galaxies: Chemical and Radiative Conditions. , 712(1):L69–L72.

Schleicher, D. R. G., Spaans, M., and Glover, S. C. O. (2010b). Black Hole Formation in Primordial Galaxies: Chemical and Radiative Conditions. , 712(1):L69–L72.

Schneider, R. and Omukai, K. (2010). Metals, dust and the cosmic microwave background: fragmentation of high-redshift star-forming clouds. , 402(1):429–435.

Schneider, R., Omukai, K., Inoue, A. K., and Ferrara, A. (2006). Fragmentation of star-forming clouds enriched with the first dust. , 369(3):1437–1444.

Schödel, R., Feldmeier, A., Neumayer, N., Meyer, L., and Yelda, S. (2014). The nuclear cluster of the Milky Way: our primary testbed for the interaction of a dense star cluster with a massive black hole. *Classical and Quantum Gravity*, 31(24):244007.

Serenelli, A., Weiss, A., Aerts, C., Angelou, G. C., Baroch, D., Bastian, N., Beck, P. G., Bergemann, M., Bestenlehner, J. M., Czekala, I., Elias-Rosa, N., Escorza, A., Van Eylen, V., Feuillet, D. K., Gandolfi, D., Gieles, M., Girardi, L., Lebreton, Y., Lodieu, N., Martig, M., Miller Bertolami, M. M., Mombarg, J. S. G., Morales, J. C., Moya, A., Nsamba, B., Pavlovski, K., Pedersen, M. G., Ribas, I., Schneider, F. R. N., Silva Aguirre, V., Stassun, K. G., Tolstoy, E., Tremblay, P.-E., and Zwintz, K. (2021). Weighing stars from birth to death: mass determination methods across the HRD. , 29(1):4.

Seth, A. C., Blum, R. D., Bastian, N., Caldwell, N., and Debattista, V. P. (2008). The Rotating Nuclear Star Cluster in NGC 4244. , 687(2):997–1003.

Seth, A. C., Cappellari, M., Neumayer, N., Caldwell, N., Bastian, N., Olsen, K., Blum, R. D., Debattista, V. P., McDermid, R., Puzia, T., and Stephens, A. (2010). The NGC 404 Nucleus: Star Cluster and Possible Intermediate-mass Black Hole. , 714(1):713–731.

Shankar, F., Bernardi, M., Sheth, R. K., Ferrarese, L., Graham, A. W., Savorgnan, G., Allevato, V., Marconi, A., Läsker, R., and Lapi, A. (2016). Selection bias in dynamically measured supermassive black hole samples: its consequences and the quest for the most fundamental relation. , 460(3):3119–3142.

Shapiro, S. L. (2005). Spin, Accretion, and the Cosmological Growth of Supermassive Black Holes. , 620(1):59–68.

Shen, Y., Wu, J., Jiang, L., Bañados, E., Fan, X., Ho, L. C., Riechers, D. A., Strauss, M. A., Venemans, B., Vestergaard, M., Walter, F., Wang, F., Willott, C., Wu, X.-B., and Yang, J. (2019). Gemini GNIRS Near-infrared Spectroscopy of 50 Quasars at z $\gtrsim$ 5.7. , 873(1):35.

Shields, J. C., Walcher, C. J., Böker, T., Ho, L. C., Rix, H.-W., and van der Marel, R. P. (2008). An Accreting Black Hole in the Nuclear Star Cluster of the Bulgeless Galaxy NGC 1042. , 682(1):104–109.

Shu, F. H. (1991). *The physics of astrophysics. Volume 1: Radiation.*

Spergel, D. N., Verde, L., Peiris, H. V., Komatsu, E., Nolta, M. R., Bennett, C. L., Halpern, M., Hinshaw, G., Jarosik, N., Kogut, A., Limon, M., Meyer, S. S., Page, L., Tucker, G. S., Weiland, J. L., Wollack, E., and Wright, E. L. (2003). First-Year Wilkinson Microwave Anisotropy Probe (WMAP) Observations: Determination of Cosmological Parameters. , 148(1):175–194.

Spitzer, Lyman, J. (1969). Equipartition and the Formation of Compact Nuclei in Spherical Stellar Systems. , 158:L139.

Spitzer, L. (1987). *Dynamical evolution of globular clusters.*

Spurzem, R. (1999). Direct N-body Simulations. *Journal of Computational and Applied Mathematics*, 109:407–432.

Stacy, A., Bromm, V., and Lee, A. T. (2016). Building up the Population III initial mass function from cosmological initial conditions. , 462(2):1307–1328.

Stone, N. C., Küpper, A. H. W., and Ostriker, J. P. (2017). Formation of massive black holes in galactic nuclei: runaway tidal encounters. , 467(4):4180–4199.

Suazo, M., Prieto, J., Escala, A., and Schleicher, D. R. G. (2019). The Role of Gas Fragmentation During the Formation of Supermassive Black Holes. , 885(2):127.

Tagawa, H., Haiman, Z., and Kocsis, B. (2020). Formation and Evolution of Compact-object Binaries in AGN Disks. , 898(1):25.

Tan, J. C. and McKee, C. F. (2004). The Formation of the First Stars. I. Mass Infall Rates, Accretion Disk Structure, and Protostellar Evolution. , 603(2):383–400.

Thomas, J., Ma, C.-P., McConnell, N. J., Greene, J. E., Blakeslee, J. P., and Janish, R. (2016). A 17-billion-solar-mass black hole in a group galaxy with a diffuse core. , 532(7599):340–342.

Tolstoy, E. and Davies, R. (2019). *MICADO Science Case, ELT-PLA-MCD-56305-0006-1.*

Tremaine, S., Gebhardt, K., Bender, R., Bower, G., Dressler, A., Faber, S. M., Filippenko, A. V., Green, R., Grillmair, C., Ho, L. C., Kormendy, J., Lauer,

T. R., Magorrian, J., Pinkney, J., and Richstone, D. (2002). The Slope of the Black Hole Mass versus Velocity Dispersion Correlation. , 574(2):740–753.

Valiante, R., Schneider, R., Volonteri, M., and Omukai, K. (2016). From the first stars to the first black holes. , 457(3):3356–3371.

Varri, A. L. and Bertin, G. (2012). Self-consistent models of quasi-relaxed rotating stellar systems. , 540:A94.

Venemans, B. P., Findlay, J. R., Sutherland, W. J., De Rosa, G., McMahon, R. G., Simcoe, R., González-Solares, E. A., Kuijken, K., and Lewis, J. R. (2013). Discovery of Three z $>$ 6.5 Quasars in the VISTA Kilo-Degree Infrared Galaxy (VIKING) Survey. , 779(1):24.

Vergara, M. Z. C., Schleicher, D. R. G., Boekholt, T. C. N., Reinoso, B., Fellhauer, M., Klessen, R. S., and Leigh, N. W. C. (2021). Stellar collisions in flattened and rotating Pop. III star clusters. *arXiv e-prints*, page arXiv:2104.01451.

Volonteri, M. (2010). Formation of supermassive black holes. , 18(3):279–315.

Volonteri, M., Haardt, F., and Madau, P. (2003). The Assembly and Merging History of Supermassive Black Holes in Hierarchical Models of Galaxy Formation. , 582(2):559–573.

Volonteri, M., Lodato, G., and Natarajan, P. (2008a). The evolution of massive black hole seeds. , 383(3):1079–1088.

Volonteri, M., Lodato, G., and Natarajan, P. (2008b). The evolution of massive black hole seeds. , 383(3):1079–1088.

Wang, F., Wang, R., Fan, X., Wu, X.-B., Yang, J., Neri, R., and Yue, M. (2019). Spatially Resolved Interstellar Medium and Highly Excited Dense Molecular Gas in the Most Luminous Quasar at z = 6.327. , 880(1):2.

Wang, L., Spurzem, R., Aarseth, S., Giersz, M., Askar, A., Berczik, P., Naab, T., Schadow, R., and Kouwenhoven, M. B. N. (2016). The DRAGON simulations: globular cluster evolution with a million stars. , 458(2):1450–1465.

Wang, L., Spurzem, R., Aarseth, S., Nitadori, K., Berczik, P., Kouwenhoven, M. B. N., and Naab, T. (2015). NBODY6++GPU: ready for the gravitational million-body problem. , 450(4):4070–4080.

Watkins, L. L., van der Marel, R. P., Bellini, A., and Anderson, J. (2015). Hubble Space Telescope Proper Motion (HSTPROMO) Catalogs of Galactic Globular Cluster. II. Kinematic Profiles and Maps. , 803(1):29.

Wehner, E. H. and Harris, W. E. (2006). From Supermassive Black Holes to Dwarf Elliptical Nuclei: A Mass Continuum. , 644(1):L17–L20.

Wise, J. H., Turk, M. J., and Abel, T. (2008). Resolving the Formation of Protogalaxies. II. Central Gravitational Collapse. , 682(2):745–757.

Woods, T. E., Agarwal, B., Bromm, V., Bunker, A., Chen, K.-J., Chon, S., Ferrara, A., Glover, S. C. O., Haemmerlé, L., Haiman, Z., Hartwig, T., Heger, A., Hirano, S., Hosokawa, T., Inayoshi, K., Klessen, R. S., Kobayashi, C., Koliopanos, F., Latif, M. A., Li, Y., Mayer, L., Mezcua, M., Natarajan, P., Pacucci, F., Rees, M. J., Regan, J. A., Sakurai, Y., Salvadori, S., Schneider, R., Surace, M., Tanaka, T. L., Whalen, D. J., and Yoshida, N. (2019). Titans of the early Universe: The Prato statement on the origin of the first supermassive black holes. , 36:e027.

Wu, X.-B., Wang, F., Fan, X., Yi, W., Zuo, W., Bian, F., Jiang, L., McGreer, I. D., Wang, R., Yang, J., Yang, Q., Thompson, D., and Beletsky, Y. (2015). An ultraluminous quasar with a twelve-billion-solar-mass black hole at redshift 6.30. , 518(7540):512–515.

Yoshida, N., Omukai, K., Hernquist, L., and Abel, T. (2006). Formation of Primordial Stars in a ΛCDM Universe. , 652(1):6–25.